NEAR-THRESHOLD KAON PAIR PRODUCTION IN PROTON-PROTON COLLISIONS

Damian Gil

A doctoral dissertation prepared in
the Faculty of Physics, Astronomy and Applied Computer Science
of the Jagiellonian University under the supervision
of Prof. Jerzy Smyrski

Cracow 2018

PRZYPROGOWA PRODUKCJA PAR NAŁADOWANYCH KAONÓW W ZDERZENIACH DWÓCH PROTONÓW

Damian Gil

Rozprawa doktorska przygotowana na
Wydziale Fizyki, Astronomii i Informatyki Stosowanej
Uniwersytetu Jagiellońskiego pod opieką
prof. dr. hab. Jerzego Smyrskiego

Kraków 2018

Wydział Fizyki, Astronomii i Informatyki Stosowanej
Uniwersytet Jagielloński

Oświadczenie

Ja niżej podpisany Damian Gil doktorant Wydziału Fizyki, Astronomii i Informatyki Stosowanej Uniwersytetu Jagiellońskiego oświadczam, że przedłożona przeze mnie rozprawa doktorska pt. „*Near-threshold kaon pair production in proton-proton collisions*" jest oryginalna i przedstawia wyniki badań wykonanych przeze mnie osobiście, pod kierunkiem prof. dr. hab. Jerzego Smyrskiego. Pracę napisałem samodzielnie.

Oświadczam, że moja rozprawa doktorska została opracowana zgodnie z Ustawą o prawie autorskim i prawach pokrewnych z dnia 4 lutego 1994 r. (Dziennik Ustaw 1994 nr 24 poz. 83 wraz z późniejszymi zmianami).

Jestem świadom, że niezgodność niniejszego oświadczenia z prawdą ujawniona w dowolnym czasie, niezależnie od skutków prawnych wynikających z ww. ustawy, może spowodować unieważnienie stopnia nabytego na podstawie tej rozprawy.

Kraków, dnia 27 września 2018 roku ……………………………………

podpis doktoranta

Rodzicom

Abstract

Measurements of the pp $\rightarrow$ ppK^+K^- reaction close to the kinematical threshold allow the studies of the K^+K^-, pK^+ and pK^- interactions in the final state. Therefore, these measurements can help to understand the nature of the $f_0(980)$ and $a_0(980)$ mesons which, according to some theoretical models, are kaonic molecules, and of the $\Lambda(1405)$ hyperon which is considered as a pK^- bound state.

In the framework of the present work, measurement of the total cross section for the pp $\rightarrow$ ppK^+K^- reaction at incident beam momentum of 3.316 GeV/*c*, corresponding to the excess energy of only 4.5 MeV, was performed.

The measurement was done at the internal proton beam of the COSY accelerator in Jülich Research Centre in Germany using the COSY-11 detection system. The integrated luminosity, determined using a coincidence measurement of the elastically scattered protons, was 1.52 pb^{-1}. In the absence of ppK^+K^- events observed in the experiment, an upper limit at 95% level of confidence on the pp $\rightarrow$ ppK^+K^- total cross section of 0.070 nb has been determined.

This limit lies below theoretical calculations taking into account the pp, pK^- and K^+K^- final-state interactions and describing the experimental data available higher above the threshold. This can indicate the influence of the Coulomb interaction which was not fully included in the theoretical calculations or absorption of kaons due to formation of the K^+K^- bound state.

Streszczenie

Pomiary reakcji pp → ppK^+K^- blisko progu kinematycznego pozwalają na badanie oddziaływań w stanie końcowym pomiędzy parami cząstek K^+K^-, pK^+ oraz pK^-. Dlatego mogą one pomóc w zrozumieniu natury mezonów $f_0(980)$ i $a_0(980)$, które według niektórych modeli teoretycznych są molekułami kaonowymi, a także struktury hiperonu $\Lambda(1405)$, który jest prawdopodobnie stanem związanym pK^-.

Poniższa rozprawa opisuje pomiar całkowitego przekroju czynnego na reakcję pp → ppK^+K^- przy pędzie padającej wiązki protonów równym 3,316 GeV/*c*, który odpowiada energii nad progiem w układzie środka masy równej zaledwie 4,5 MeV.

Eksperyment został przeprowadzony z wykorzystaniem układu detekcyjnego COSY-11 pracującego na wewnętrznej wiązce protonów akceleratora COSY w Centrum Badawczym Juelich w Niemczech. Całkowita świetlność, wyznaczona w oparciu o równolegle prowadzony pomiar rozpraszania elastycznego protonów, wyniosła 1,52 pb^{-1}. Z powodu niezaobserwowania zdarzeń typu ppK^+K^-, wyznaczono górną granicę przekroju czynnego na badaną reakcję, która na poziomie ufności 95% wynosi 0,070 nb.

Granica ta leży poniżej przewidywań teoretycznych, uwzględniających oddziaływanie w stanie końcowym pomiędzy pp, pK^- oraz K^+K^-, które dobrze opisują dane eksperymentalne przy wyższych energiach nad progiem. Fakt ten może wskazywać na istotną rolę oddziaływania kulombowskiego, które nie zostało w pełni uwzględnione w opisie teoretycznym, lub na absorpcję kaonów, spowodowaną powstaniem stanu związanego K^+K^-.

Table of contents

Chapter 1

Introduction

Measurements of meson production in the elementary proton-proton collisions close to the kinematical threshold are an important tool to study the production mechanism as well as the interaction of mesons with other particles in the final state. Due to the proximity of the threshold, the orbital momenta of particles in the final state are dominated by the lowest possible values, which simplifies the theoretical description of the studied process. In turn the low relative momenta between particles in the final state lead to a strong interaction between the particles in the case of existence of bound or quasi-bound states.

The main difficulty of the experimental studies of the near-threshold reactions are low values of the production cross sections, resulting from a small phase space volume accessible for the reaction products. A strong attractive interaction between particles in the final state (e.g. the nuclear force between two nucleons) increases the cross section and a repulsive interaction (e.g. the Coulomb force between two protons) decreases it. This increase (or decrease) of the production cross section, resulting from the interaction between particles in the final state, is usually described by the so-called enhancement factor. In the near-threshold region, this factor can be parameterized in the finite range approximation by the scattering length and the effective range parameters which describe the interaction between the particles at low energies. In this way the comparison of experimental cross sections with theoretical calculations including the enhancement factor gives the possibility to determine these parameters.

The COSY-11 detection system [1] at the COSY accelerator in the Jülich Research Centre in Germany was designed for measurements of the near-threshold production of light mesons, with masses below 1 GeV/c^2, in proton-proton and proton-deuteron collisions. The detector operated between 1993 and 2007 and provided numerous data on the production of η, K^+, ω and η' mesons. Analysis of these data led, among others, to the determination of the η-d and η'-p scattering length (see Refs. [2] and [3] respectively). An overview of the COSY-11 results can be found in Ref. [4].

One of the main research topics of COSY-11 was the near-threshold production of K^+K^- pairs in proton-proton collisions. The motivation for these studies was connected with the unknown nature of the $f_0(980)$ and $a_0(980)$ mesons. The masses of these particles are very close to the mass of the kaon pair (987 MeV) and some of the theoretical models of the structure of these states describe them as bound states of two kaons [5]. Measurements of the $pp \rightarrow ppK^+K^-$ reaction close to threshold make it possible to study the K^+K^- interaction at low energies which is essential for making conclusions about possible binding. These measurements also allow the investigation of the pK^+ and pK^- interactions. The knowledge of them is essential for studies of the properties of kaons inside dense baryonic matter. The strength of the pK^- interaction is also important for understanding the structure of the $\Lambda(1405)$ hyperon which can be considered as a pK^- bound state [6].

The existing data for the total cross section for the kaon pair production in proton-proton collisions for excess energies below the φ meson production threshold (i.e. 32 MeV) include five data points from COSY-11 [7–10] and one data point from the ANKE collaboration [11]. The point from COSY-11 closest to the threshold, at excess energy $Q = 3$ MeV, is only an upper limit on the total cross section, because there were no $pp \rightarrow ppK^+K^-$ events observed. Due to relatively large uncertainties of the experimental total cross sections, it is not possible to determine precisely the contributions from the final-state interaction (FSI) in the ppK^+K^- system. This concerns especially the pK^- and K^+K^- interactions which are weaker than the pp one. So far the pK^+ interaction is not included in the description of the data because it is substantially weaker than the pK^- one.

To improve the precision of studying the effects of the pK^- and K^+K^- interactions, which are the strongest near the threshold, the COSY-11 collaboration performed a measurement of the $pp \rightarrow ppK^+K^-$ reaction very close to the threshold, at an excess energy of 4.5 MeV. The present thesis is devoted to analysis of the data from this experiment. The paper consists of six chapters and is organized as follows. In the next (second) chapter more details about the physics motivation of the performed measurement are given. Description of the experimental setup, including the COSY accelerator and the COSY-11 detection system, is given in Chapter 3. Chapter 4 presents consecutive steps of the ppK^+K^- data analysis, including detector calibration, event selection, determination of luminosity and of the total cross section for the $pp \rightarrow ppK^+K^-$ reaction, as well as its comparison with theoretical models including description of the final-state interaction. In Chapter 5 analysis of the reactions $pp \rightarrow ppX$ with $X = \omega, \eta'$ is described. These reactions were registered parallel to the K^+K^- production channel. Obtained total cross sections for the ω and η' meson production are compared with results from other experiments and with predictions of theoretical models. In particular this comparison is used as a cross-check of the luminosity determination. The thesis is summarized in Chapter 6.

Chapter 2

Physics motivation

The $pp \to ppK^+K^-$ total and differential cross sections close to threshold are very sensitive to the interactions between particles in the final state, and therefore are well suited for studies of them. There are many interesting topics connected with properties of the dynamics between the final-state kaons and protons. Knowledge of the K^+K^- interaction is of high importance for understanding the structure of the scalar mesons $f_0(980)$ and $a_0(980)$ which according to some theoretical models are $K\bar{K}$ molecules. In turn the pK^- dynamics is interesting from the point of view of study of the nature of the $\Lambda(1405)$ hyperon which is considered as a pK^- molecular state.

Experimental data on the kaon pair production in the elementary proton-proton collisions are very important for interpretation of the data for the production of kaons in heavy ion collisions and understanding the properties of kaons inside dense baryonic matter.

The above issues are presented in more detail in the next three sections of this chapter. In the fourth section existing experimental data on the near-threshold $pp \to ppK^+K^-$ cross sections and their comparison with selected theoretical predictions of models, describing the reaction mechanism and the interactions between particles in the final state, are presented.

2.1 Structure of the $f_0(980)$ and $a_0(980)$ mesons

A primary motivation for measuring the $pp \to ppK^+K^-$ reaction close to the kinematical threshold at COSY-11 was the hope to solve one of the most intriguing puzzles of the hadron physics which is the structure of the $f_0(980)$ and $a_0(980)$ mesons. These are scalar mesons with the quantum numbers $J^{PC} = 0^{++}$. The $f_0(980)$ is an isoscalar ($I = 0$), while $a_0(980)$ is an isovector ($I = 1$) state. The dominant decay channel for the $f_0(980)$ and $a_0(980)$ is $\pi\pi$ and $\eta\pi$, respectively.

In the quark model, these mesons are described as orbitally excited $q\bar{q}$ states with orbital momentum $L = 1$. However, interpretation of the f_0 and a_0 mesons as quarkantiquark systems creates a number of difficulties (see, e.g. Ref. [5]). For example, the relatively small total widths of the f_0 and a_0, which are on the order of several tens of MeV [12], are much smaller than ∼500 MeV expected from the quark model [5]. A number of models that interpret these resonances as non-$q\bar{q}$ states have been proposed. In 1977 Jaffe suggested a $qq\bar{q}\bar{q}$ interpretation of them [13]. The proximity of the $f_0(980)$ and $a_0(980)$ masses to the $K^0\bar{K}^0$ threshold (995 MeV) suggests that they may be bound states of two kaons, the so-called $K\bar{K}$ molecules. The first of many models describing them as $K\bar{K}$ molecule was proposed by Weinstein and Isgur in 1990 [5]. There are also interpretations of the $f_0(980)$ and $a_0(980)$ as superposition of $qq\bar{q}\bar{q}$ states and other components, such as $K\bar{K}$ (see, e.g. Ref. [14]). An overview of different interpretations of these states can be found in Ref. [12] on page 864 and 1495.

2.2 Nature of the $\Lambda(1405)$ hyperon

According the Particle Data Group [12] the $\Lambda(1405)$ is a well established four-star baryon with isospin 0, spin $\frac{1}{2}$ and a negative parity. It decays primarily into a $\Sigma\pi$ pair and has a width of $\Gamma = 50$ MeV. However, the nature of this particle is still discussed and remains unclear [15].

In the quark model, $\Lambda(1405)$ hyperon is described as a system of three quarks (uds) with one of the quarks excited to $L = 1$ orbital momentum state. This excitation results in the negative parity of the system. The big and still unresolved mystery is its low mass. Despite the content of the s quark, the $\Lambda(1405)$ is lighter than the N(1535) baryon, the first excited state of the nucleon with identical spin and parity ($\frac{1}{2}^-$).

Already in the 1960s, Dalitz and co-workers [6] suggested that $\Lambda(1405)$ is a bound state of an $\bar{K}$ and a nucleon. Such a state is also referred to as a $\bar{K}N$ molecular state. Also a new lattice QCD simulation results indicate its molecular nature [16]. The mass of the hyperon lies below the sum of K^- and p masses (1432 MeV) and the K^0 and n masses (1437 MeV). In the case of binding of these pairs of particles, the binding energy would be 27 and 32 MeV respectively.

The possible binding of the $\bar{K}N$ pair is associated with a strong attractive interaction between $\bar{K}$ and N. This interaction is studied based on experimental data from the elastic pK^- scattering and from the energy levels of the kaonic hydrogen (see, e.g. Refs. [17–19]). The low energy parameters describing this interaction can be also determined based on the effects of the FSI observed in the $pp \to ppK^+K^-$ reaction.

The study of the $\bar{K}N$ interaction is also of high interest from the point of view of the search for kaonic nuclei [20,21].

2.3 Properties of kaons inside dense baryonic matter

The information about processes occurring during relativistic heavy ion collisions, especially properties of nuclear matter at high densities, can be gained by registration of the K^+ and K^- mesons which are created in the fireball region and observation of their abundance and phase space distributions [22]. But learning about the dense baryonic matter and the properties of strange particles immersed in it from the observation of yields and momentum distributions of kaons is impossible without knowledge about their production in the elementary nucleon-nucleon collisions.

One of the examples of the information coming from the comparative researches of the strangeness production in the elementary nucleon-nucleon collisions and heavy ion collisions was provided by the KAOS collaboration. They observed that the multiplicity of K^+ per participating nucleon produced in the C+C or Ni+Ni collisions is almost the same as for K^- at the corresponding centre of mass energy above threshold (with respect to nucleon-nucleon kinematics), whereas in elementary proton-proton collisions the multiplicity of K^+ mesons is two orders of magnitude larger than that of K^- [23] (see Fig. 2.1). One interpretation of these observations is that in nuclear matter kaons undergo a repulsion, whereas antikaons feel a strong attractive potential, which results in a splitting of their effective masses. This effect is even more pronounced when taking into account the fact that K^+ are much less absorbed than K^- in nuclear matter, because the latter excite hyperon resonances which can decay into pion-nucleon pairs in weak processes.

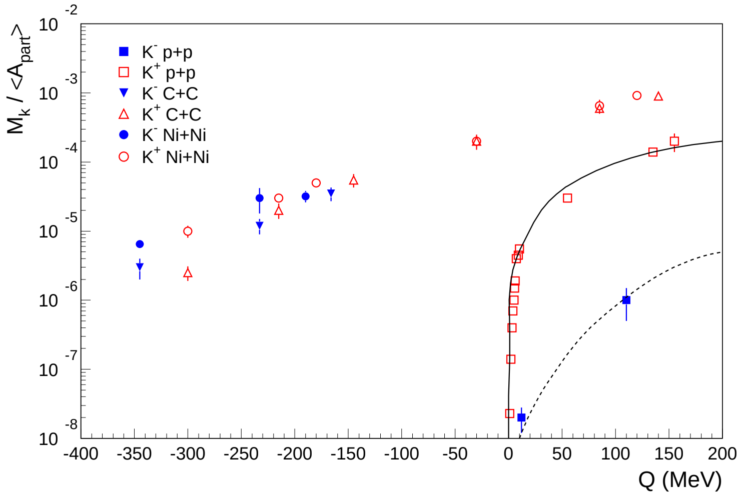

Figure 2.1: Multiplicity of K^+ and K^- production per participating nucleon for C+C, Ni+Ni and proton-proton collisions. Figure adopted from Ref. [23].

One of the ways to better understand the medium modification of the kaon properties is to study how the presence of a second nucleon or hyperon would influence the pK^+ or pK^-. This can be studied by measuring the energy dependence of the total cross section for the reaction $pp \to ppK^+K^-$ close to the kinematical threshold.

2.4 Excitation function for the $pp \to ppK^+K^-$ reaction

The first measurement of the $pp \to ppK^+K^-$ reaction made by the COSY-11 collaboration was performed in 1997. The data was taken for an excess energy of Q = 6 MeV and the integrated luminosity was 0.079 pb^{-1}. Only two events of the kaon pair production were registered, and therefore the obtained value of the total cross section $\sigma = 490\ ^{+400}_{-370}$ pb [7] was hindered by large uncertainty.

The further measurements were performed for excess energies Q = 3 MeV and Q = 17 MeV with integrated luminosity of 0.84 pb^{-1} and 4.5 pb^{-1}, respectively [9]. In the measurement at lower energy, no $pp \to ppK^+K^-$ events were observed which allowed determination of only the upper limit on the total cross section to be equal to 0.16 nb at the confidence level CL = 95%. At Q = 17 MeV the total cross section was $1.8 \pm 0.27\ ^{+0.28}_{-0.35}$ nb.

Two more measurements the COSY-11 collaboration performed at Q = 10 MeV and Q = 28 MeV with integrated luminosity 2.77 pb^{-1} and 2.27 pb^{-1}, respectively. Obtained results for the total cross section of 0.787 ± 0.178 ± 0.082 nb and 4.285 ± 0.977 ± 0.374 nb respectively were published in 2005 [10].

The COSY-11 data points for the $pp \to ppK^+K^-$ total cross section are presented in Fig. 2.2 together with data from other experiments measured below Q = 120 MeV, including three data points from the ANKE experiment at COSY [11, 24] and one at the highest energy (Q = 114 MeV) from the DISTO detector system at Saturne [8]. The data at higher Q have the φ meson contribution subtracted. As one can see, the total cross section grows rapidly with excess energy, for example, in the energy range from 10 to 100 MeV it increases by almost two orders of magnitude. The rapid increase of the cross section above the threshold results from the growth of the phase space volume available for the produced particles. For the four-body $pp \to ppK^+K^-$ reaction, the phase space volume is proportional to $Q^{\frac{7}{2}}$. However, the corresponding dependence of the total cross section on Q can be strongly modified by the final-state interaction.

A commonly used way of describing the effects of the FSI is application of the Watson-Migdal theorem [25, 26]. According this, the transition amplitude for a near-threshold reaction with two particles interacting strongly in the final state can be factorized as

$$M = M_0 \cdot F_{FSI}, \tag{2.1}$$

where M_0 describes the production of the particles and is equal to the transition amplitude in the absence of the FSI, while F_{FSI} is the so-called enhancement factor, describing the enlargement of the transition amplitude due to the final-state interaction.

For orbital momentum equal to zero, this factor can be approximated by the inverse of the Jost function:

$$F_{\mathrm{FSI}} = \frac{1}{f_0(k)}, \tag{2.2}$$

where k is the relative momentum of the two particles interacting strongly in the final state. In the effective range approximation the Jost function has the form [27]:

$$f_0(k) = \frac{k + i\beta}{k - i\alpha}, \tag{2.3}$$

where parameters α and β are connected with the scattering length a and the effective range b in the following way:

$$a = \frac{1}{\alpha} + \frac{1}{\beta}, \tag{2.4}$$

$$b = \frac{2}{\alpha + \beta}. \tag{2.5}$$

At small momenta ($k \ll \beta$), the enhancement factor is proportional to the amplitude for elastic scattering of the two particles interacting strongly in the final state:

$$F_{\mathrm{FSI}} \sim \frac{1}{\frac{bk^2}{2} + \frac{1}{a} - ik}. \tag{2.6}$$

In the scattering length approximation this expression simplifies to:

$$F_{\mathrm{FSI}} \sim \frac{1}{1 - ika}. \tag{2.7}$$

Description of the final-state interaction in the $pp \to ppK^+K^-$ reaction is a many body problem, since it involves not only the pp, but also the pK^+ and pK^-, as well as the K^+K^-interactions. A possible simplification of this problem is provided by the approximation of the FSI enhancement factor by the product of elements for the two-body subsystems occurring in the final state. In Ref. [28] the following factorization was proposed:

$$F_{\mathrm{FSI}} = F_{pp}(k_{pp}) \cdot F_{p_1K^-}(k_{p_1K^-}) \cdot F_{p_2K^-}(k_{p_2K^-}) \cdot F_{K^+K^-}(k_{K^+K^-}). \tag{2.8}$$

In this approximation the pK^+ interaction was not included, since it is considered as repulsive and substantially weaker compared to the other effects [4]. The pp FSI was described taking into account the Coulomb interaction as:

$$F_{pp} = \frac{e^{i\delta_{pp}(^1S_0)\sin\delta_{pp}(^1S_0)}}{Ck_1}, \tag{2.9}$$

where $\delta_{pp}(^1S_0)$ is the phase shift and C is the square root of the Coulomb penetration factor.

The pK^- interaction was calculated using the scattering length approximation (Eq. 2.7) with the scattering length a = (-0.65 + 0.78i) fm [29]. The K^+K^- interaction was described using the effective range approximation (Eq. 2.3) with a = (8 + 0i) fm and b = (-0.1 + 1.2i) fm [28]. These parameters were determined using the $\mathrm{K^+K^-}$ invariant mass distributions measured at excess energies of 17 and 28 MeV. The total cross section for the pp $\to$ $\mathrm{ppK^+K^-}$ reaction was calculated assuming a constant value of the amplitude M_0 and by taking the integral of the squared module of the enhancement factor F_{FSI} over the phase space available for the reaction products. Results of the calculations are presented in Fig. 2.2 together with experimental total cross sections, measured below the φ meson production threshold (Q = 120 MeV). The four curves present the calculations corresponding to the following cases:

- the FSI is neglected and the cross section is proportional to the four-body phase space volume;
- the pp FSI is included;
- the pp and $\mathrm{pK^-}$ FSI are included;
- the pp, $\mathrm{pK^-}$and $\mathrm{K^+K^-}$ FSI are included.

All curves were normalized to the experimental point at Q = 114 MeV.

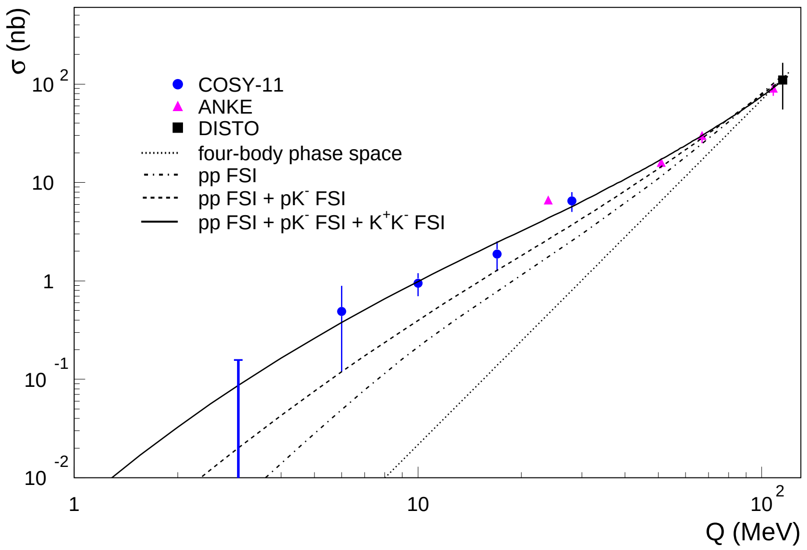

Figure 2.2: The pp $\to$ $\mathrm{ppK^+K^-}$ total cross section measured in previous experiments [7–11, 24] and theoretical curves from [28] describing the FSI as presented in the text.

Only the curve presenting the calculation including all the interactions (pp, $\mathrm{pK^-}$and $\mathrm{K^+K^-}$) properly describes the data points. From the figure one can also conclude that the theoretical results are very sensitive to details of the FSI at energies very close to the threshold (Q less than about 10 MeV). Additional data points at this low energies would substantially improve the precision of determining the strength of the final-state interaction, in particular the $\mathrm{pK^-}$ and $\mathrm{K^+K^-}$ FSI.

Chapter 3

Experimental setup

3.1 The COSY facility

The COoler SYnchrotron (COSY) [30], located in the Jülich Research Centre in Germany, accelerates and stores unpolarized and polarized protons and deuterons in the momentum range between 300 MeV/c and 3.7 GeV/c. Figure 3.1 presents a schematic view of the COSY accelerator complex. Ion sources provide polarized or alternatively unpolarized ions of H^- or D^- which are next preaccelerated in the injector cyclotron. After preacceleration, the H^- ions of energy 45 MeV or 75 MeV D^- ions are extracted [31] to the 100 m long beamline to be injected into the storage ring COSY via stripping injection. The circumference of the ring is 183.4 m. It contains 24 dipole magnets arranged along two arcs, and two straight sections of about 40 m length each. The COSY can be filled with up to 10^{11} particles and is equipped with two independent cooling systems - electron cooling and stochastic cooling - which allow the reduction of the momentum and spatial spread of the beam [32].

The electron cooling is used mainly at the injection energy, whereas the stochastic cooling works at higher beam momentum, in the range between 1.5 and 3.7 GeV/c. For the electron cooling, a beam of electrons is merged with the proton beam on a path of about 1.5 m. Velocity of electrons is equal to the average velocity of the protons, but the temperature of electrons, connected with their velocity spread, is much smaller than the one of protons. Due to the Coulomb scattering of protons in the electron gas, they cool down and their velocity spread is reduced. It results in reduction of the emmitance of the beam.

The system of stochastic cooling at COSY contains two pickup electrodes which measure the horizontal and vertical deviations of beam bunches from ideal orbit. These deviations are then corrected with two kickers. The cooling reduces the beam emmitance and the longitudinal momentum spread of the beam. It also counteracts beam losses due to heating of it caused by interactions with targets of internal experiments. The COSY beam is available for internal experiments, but it can be also extracted to external detec-

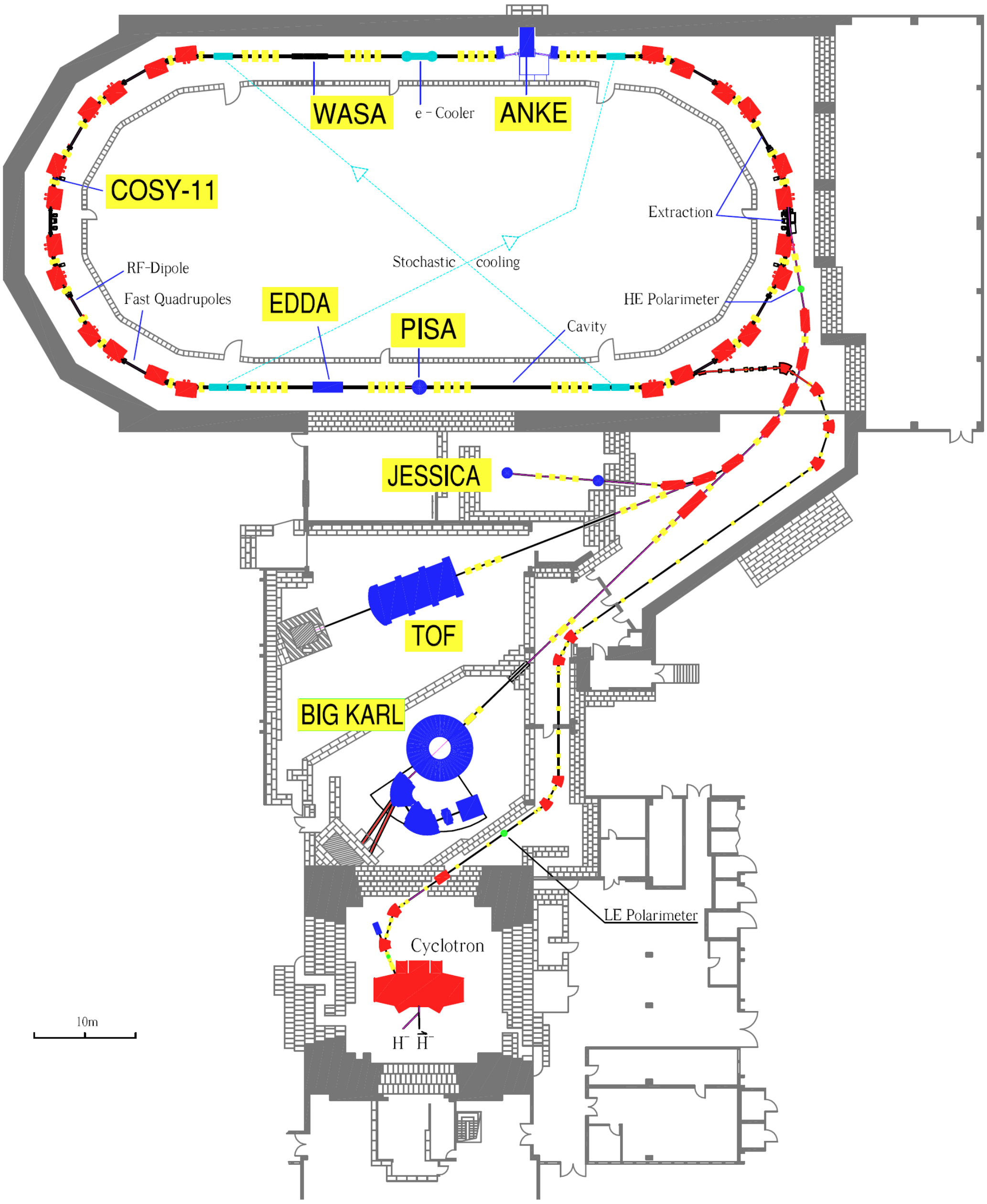

Figure 3.1: Floor plan of the COSY facility [4]. The COSY-11 detection system is installed on one of the two arc-shaped sections of the ring.

tion systems. One of the internal experiments is COSY-11. Its schematic view together with COSY facility elements is presented in Fig. 3.2.

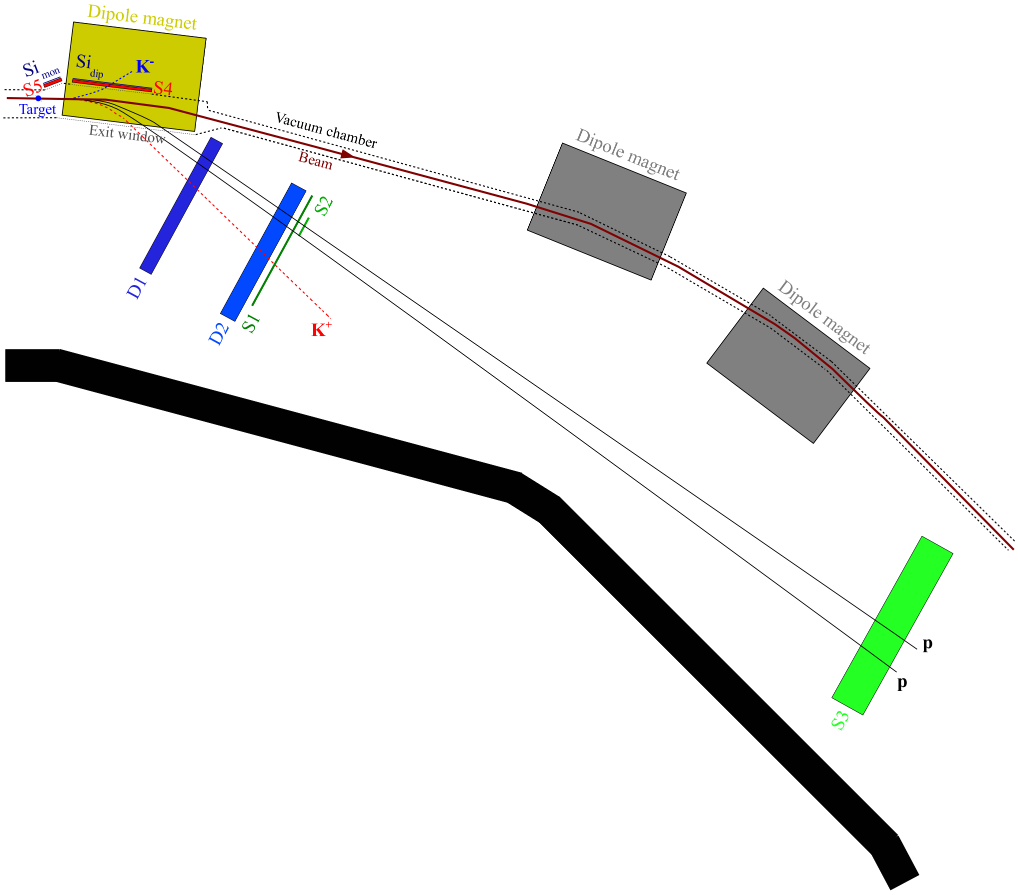

Figure 3.2: The COSY-11 detection setup and its location at the COSY facility. The black rectangle is the wall on the inside of the ring. Tracks of the $pp \rightarrow ppK^+K^-$ reaction products obtained in a simulation of this reaction are also indicated.

3.2 The COSY-11 detection system

The present measurements were performed with the COSY-11 detection system, schematically presented in Fig. 3.3. The internal proton beam of the COSY is scattered on the COSY-11 H_2 cluster target. The target is installed in the front of a standard COSY dipole magnet of C-type. Charged reaction products emitted from the target at small angles with respect to the beam direction are momentum analysed in the field of the magnet.

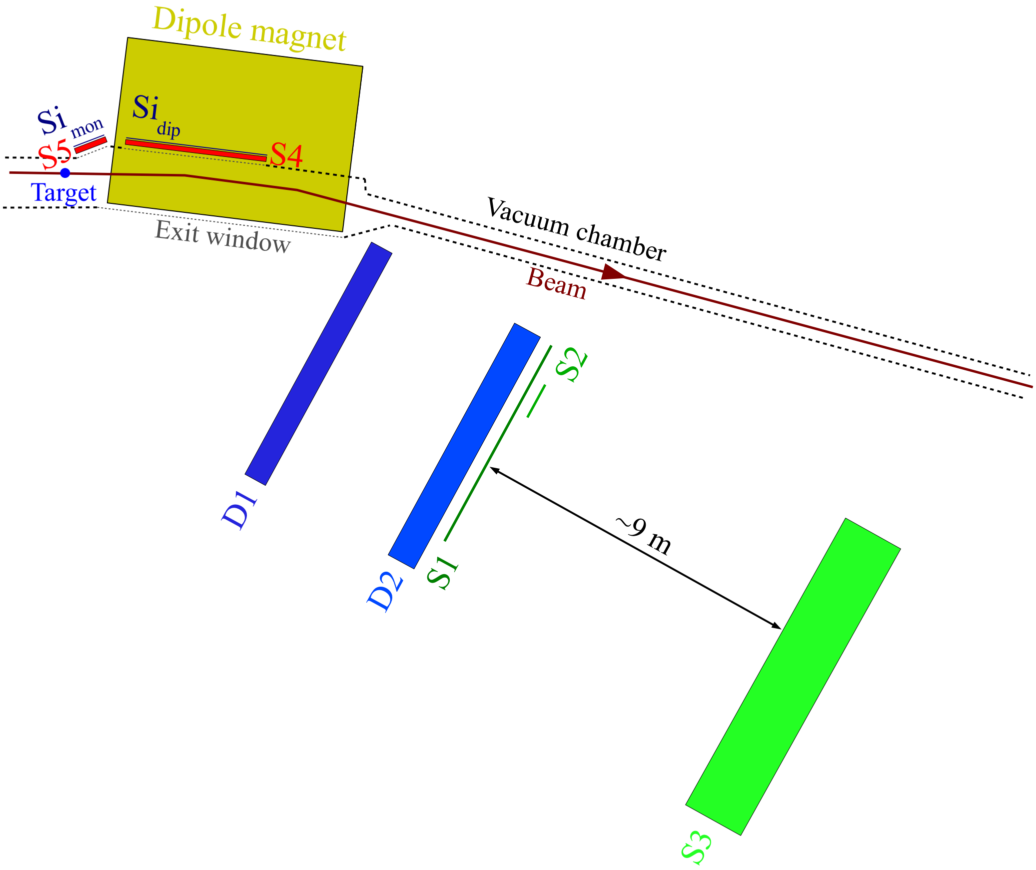

Figure 3.3: The COSY-11 detection system.

Produced positively charged particles are deflected outside the COSY vacuum chamber and are registered in a set of two drift chambers D1 and D2. Identification of particles is based on the time-of-flight (ToF) measurement on a path of about 9.1 m between scintillation hodoscopes S1 and S3. For resolving two close proton tracks, a fine granularity hodoscope S2 is placed behind the S1 detector. It is also used in the ToF measurements.

For detection of the negatively charged reaction products, the system comprises scintillation hodoscope S4 and position sensitive silicon pad detector $\mathrm{Si}_{\mathrm{dip}}$, both located inside the dipole magnet gap.

Luminosity in the experiment is monitored using a coincidence measurement of the elastically scattered protons. For this the forward scattered protons are registered in the drift chambers D1 and D2, while the recoil protons are detected with scintillation hodoscope S5 and position sensitive silicon pad detector $\mathrm{Si}_{\mathrm{mon}}$ placed near the target.

A general description of the COSY-11 cluster target and the component detectors is given in the following subsections. A more detailed description can be found in Ref. [1].

3.2.1 Cluster target

COSY-11 uses an internal hydrogen target of the cluster type [33, 34]. Application of the internal target allows one to profit from the high quality of the internal accelerator beam. The heating of the beam by the interaction in the target is counteracted by the stochastic cooling. The high frequency of the beam circulation in the COSY ring compensates for a relatively low density of the internal target of typically 10^{14} atoms per cm^2 and allows one to reach sufficiently high luminosity of 10^{30} cm^{-2} s^{-1} with 10^{10} stored protons.

A schematic view of the cluster target is presented in Fig. 3.4. Precooled to 50 K and pressurized to 18 bar hydrogen is adiabatically expanded through a de Laval nozzle. As a result of the expansion, gas is cooled further and condensates in the form of clusters containing up to 10^6 hydrogen atoms. A stream of clusters is collimated with a skimmer and two further collimators. It crosses the COSY beam in a scattering chamber. A diameter of the cluster stream in the interaction region is of about 10 mm and a typical density is 10^{14} atoms per cm^3.

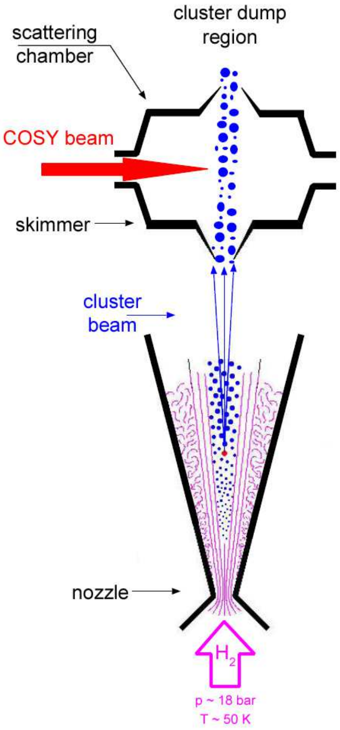

Figure 3.4: Schematic view of the COSY-11 internal cluster target [35].

3.2.2 Drift chambers D1 and D2

Particle tracking in the COSY-11 experiment is provided by two planar drift chambers D1 and D2, spaced by 70 cm. Active area of both detectors is the same: 1680 mm wide and 433 mm high. The D1 chamber contains three pairs of detection planes. Wires in the first pair are oriented vertically (i.e. 0°) and in the next two pairs are inclined at -31° and $+31^\circ$, respectively. D2 has two additional planes with vertical wires, in order to improve the position resolution in the horizontal direction. In total the chambers comprise 14 detection planes. The arrangement of the detection planes in the drift chambers is schematically shown in the left-hand side of Fig. 3.5.

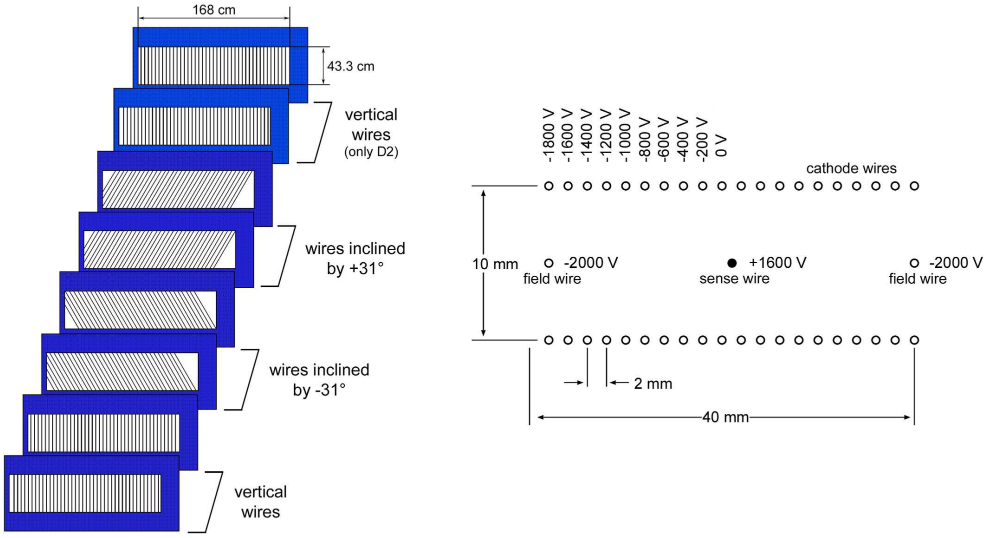

Figure 3.5: Orientation of wires in consecutive detection planes in the drift chambers (left). Drift cell structure and voltage distribution (right).

In order to resolve the left-right position ambiguity with respect to the sense wire, drift cells in consecutive planes of each pair are staggered by half of the cell width. That configuration allows the measurement of the horizontal and vertical coordinates of tracks also in a case of multi-track events.

The detection planes consist of drift cells arranged next to each other. A structure of the cell is presented in the right-hand side of Fig. 3.5. Width of the cells is equal to 40 mm which corresponds to the maximum drift path of 20 mm. A depth of the cell equals 10 mm. The anode wires, also referred to as sense wires, are made of 20 μm diameter gold-plated tungsten, while for the field wires and the cathode wires 50 μm Cu-Be is used. Charged particle passing through the cell ionizes the gas mixture, producing electron-ion pairs. The positively charged ions drift to the field wires and the cathode wires, whereas the ionization electrons drift to the sense wire. Distance between the sense wire and the particle track is determined by measuring the drift time of electrons. With applied gas mixture of 50% argon and 50% ethane at atmospheric pressure and the electric field of about 1 kV per cm, the maximum drift time is equal to about 400 ns.

During the off-line analysis of data, tracks of particles registered in D1 and D2 are reconstructed with the code MEDUZA [36]. Thanks to a high detection efficiency of the detection planes (about 98%) and some redundancy of the applied setup of the detection planes, efficiency of reconstructing particle tracks is very close to 100%.

3.2.3 Scintillation hodoscopes S1 and S2

COSY-11 contains three scintillation hodoscopes: S1, S2 and S3 which are used for:

- time-of-flight measurements,
- providing start time for the drift time determination in the drift chambers,
- triggering of read out of detectors.

The hodoscope S1 is placed directly behind the drift chamber D2 (see Fig. 3.3). It consists of sixteen scintillation modules made of BC 404 plastic with dimensions of 450 mm vertically, 100 mm horizontally and a thickness of 4 mm. The scintillator elements are oriented vertically and read out at both ends by photomultipliers. Two proton tracks hitting the same S1 module are separated by a second (movable) hodoscope S2, having a smaller width but much higher granularity than S1. It consists of sixteen modules with dimensions of 450 mm vertically, 13.5 mm horizontally and a thickness of 2 mm.

3.2.4 Scintillator wall S3

The S3 hodoscope, also called scintillator wall, serves as the stop detector in the ToF measurements, while the S1 (S2) hodoscope is used as a start detector. The S3 wall was built according the idea of the AMADEUS detector developed at the University of Bonn [37]. The S3 detector consists of a plate of BC 404 plastic scintillator with dimensions of 220 cm horizontally, 100 cm vertically and a thickness of 5 cm. The emitted scintillation light, generated inside the scintillator by charged particles, is detected by a matrix arrangement of 217 photomultipliers, with a 4 cm air gap separating the scintillator and the photomultiplier matrix, as presented in Fig. 3.6. Only a few photomultipliers within a certain cone, referred to as a cluster, show a considerable response to the particle passing through, because the amount of light registered by each photomultiplier drops off rapidly with increasing distance to the point of particle impact. This allows determination of the particle impact position by taking an average over coordinates of the photomultipliers in the cluster weighted by the height of their pulses.

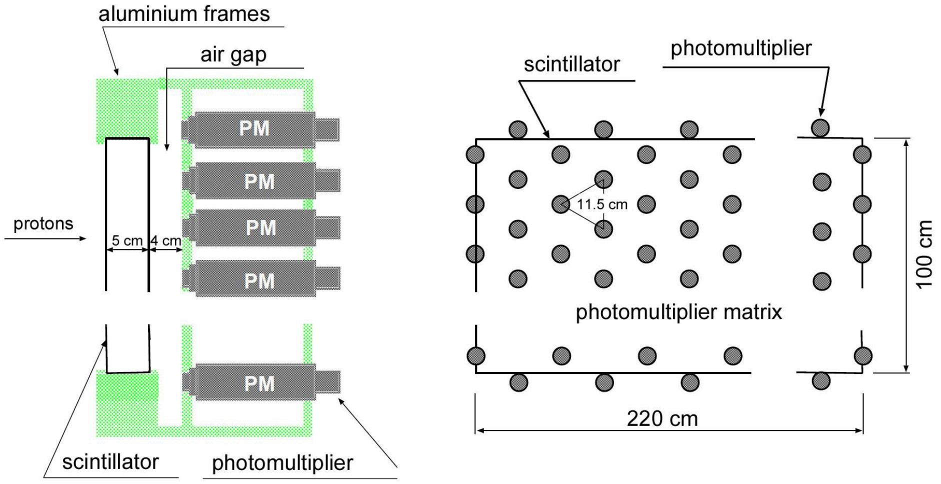

Figure 3.6: The S3 scintillation wall schematic view [38] (left). The schematic view of the photomultiplier matrix (right).

3.2.5 Silicon pad detectors

COSY-11 uses two sets of silicon pad detectors: one is the monitor detector $\mathrm{Si_{mon}}$ which detects recoil protons from the proton-proton elastic scattering; the second is detector placed inside the dipole magnet $\mathrm{Si_{dip}}$ for the detection of negatively charged mesons, especially kaons (K^-), which are diverted towards the yoke of the COSY dipole magnet. Both silicon pad detectors consist of identical segments containing four pads. Each single pad has dimensions of 22 mm vertically, 4.5 mm horizontally and a thickness of 0.28 mm.

The $\mathrm{Si_{mon}}$ consists of 36 segments arranged in three rows, the $\mathrm{Si_{dip}}$ comprises of 180 segments, also arranged in three rows. In each row the adjacent segments overlap by 1 mm and two neighboring rows overlap by 4 mm. The middle row is set backwards by 2 mm with respect to the upper and lower row (see Fig. 3.7). Altogether there are 864 silicon pads in the COSY-11 detection system. Each pad is read out separately. The $\mathrm{Si_{mon}}$ granularity allows the determination of the scattering angle for the protons with an accuracy of $\pm$ 0.5°.

3.3 Data acquisition and trigger systems

A schematic drawing of the COSY-11 data acquisition system (DAQ) [40] is shown in Fig. 3.8. Pulses from the detectors are registered with analog-to-digital converter (ADC) modules and time-to-digital converter (TDC) modules which are housed in the CAMAC and FASTBUS crates. Data from the crates are read out with computers of PC class. The synchronization of the data stream is assured by a dedicated computer, Synchronization

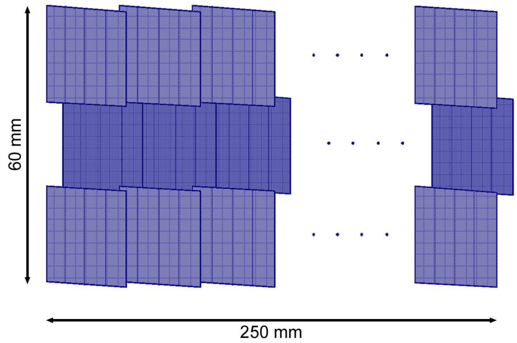

Figure 3.7: Arrangement of segments in three rows in the silicon pad detectors [39].

Master (SM). When the triggering electronics, described later in this section, generates a trigger signal and the SM accepts it, the signal is sent to the Gate Generator which provides Gate Signal for the ADC and TDC modules. That signal initializes read out of the modules. At the same time, the incremented event number is transferred to the synchronization bus and from it to the individual Synchronization Slaves (SS), until it reaches the SM again (for control purposes). Every connected PC reads out its modules (after an individual conversion time of each module). Sub-events collected in the PCs are sent by the Fast Ethernet to the Exabyte tape recorder and simultaneously to the Experiment Control computer. First analyses of the data can be carried out during the measurement (on-line) in order to check the current status of the experiment and to locate possible sources of errors promptly.

Because the DAQ bandwidth is limited to a few hundreds of Hz of events which can be saved on the tape, in measurements with high rates of particles one needs to impose some conditions excluding not interesting events from saving on the tape. That is done by the triggering electronics (trigger). In the present measurements all trigger conditions were based exclusively on the signals from the scintillation detectors. The applied trigger was an alternative of a trigger selecting the $\mathrm{pp} \rightarrow \mathrm{ppK^+K^-}$ events ($\mathrm{T_{ppKK}}$) and a trigger selecting events of the proton-proton elastic scattering ($\mathrm{T_{pp_{mon}}}$), prescaled by a factor of 64:

$$\mathrm{T} = \mathrm{T_{ppKK}} \vee \mathrm{T_{pp_{mon}}}/2^6. \tag{3.1}$$

The $\mathrm{T_{ppKK}}$ trigger was chosen as the requirement to register two charged tracks of the two outgoing protons in the scintillation hodoscopes S1, S2 and S3. It was defined as follows:

$$\mathrm{T_{ppKK}} = \left\langle \mathrm{S1}_{\mu\geq 2} \vee \left\{ \mathrm{S1}_{\mu=1} \wedge \mathrm{S1}^{3\ldots 5}_{\mathrm{high}} \wedge \left[\mathrm{S2}_{\mu\geq 2} \vee (\mathrm{S2}_{\mu=1} \wedge \mathrm{S2_{high}}) \right] \right\} \right\rangle \wedge \mathrm{S3}_{\mu_{\mathrm{PM}}\geq 3}, \tag{3.2}$$

where $\mathrm{S1}_{\mu\geq 2}$ means that there are two or more signals in S1 detector; $\mathrm{S1}_{\mu=1}$ - one signal in S1 detector; $\mathrm{S1}^{3\ldots 5}_{\mathrm{high}}$ - a signal with high amplitude in one of S1 segments from 3 to 5; $\mathrm{S2}_{\mu\geq 2}$ - two or more signals in S2 detector; $\mathrm{S2}_{\mu=1}$ - one signal in S2 detector; $\mathrm{S2_{high}}$ - a

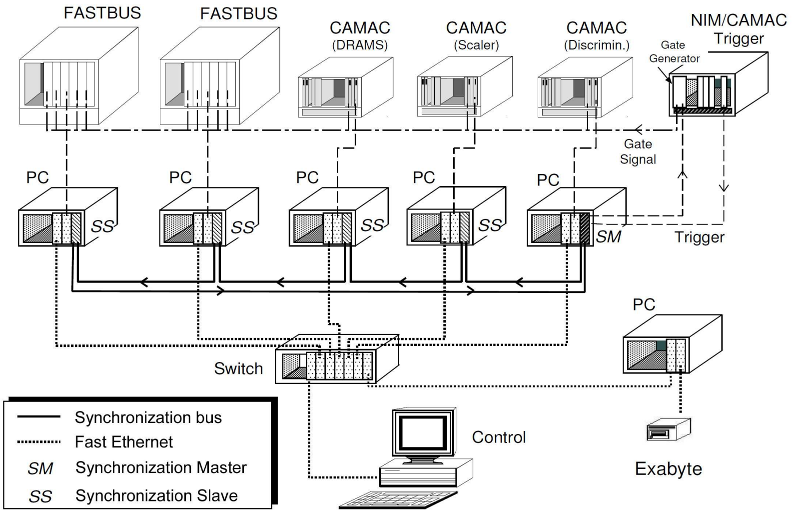

Figure 3.8: General schematics of the COSY-11 data acquisition system.

signal with high amplitude in S2 detector; $S3_{\mu_{PM} \geq 3}$ - signals in three or more photomultipliers of S3 detector.

This triggering condition can be expressed in the following equivalent way:

- signals registered in at least two S1 segments and at least three signals in S3
- or registered exactly one high amplitude signal in S1 segments from 3 to 5, and at least two signals in S2, and at least three signals in S3
- or registered exactly one high amplitude signal in S1 segments from 3 to 5, and exactly one high amplitude signal in S2, and at least three signals in S3.

The trigger selecting the pp elastic scattering was defined as a coincidence between the S1 hodoscope and the S5 scintillator:

$$T_{pp_{mon}} = S1_{\mu=1} \wedge S5. \tag{3.3}$$

This provides a coincidence measurement of the forward scattered proton and the recoil proton with the S1 hodoscope and the S5 detector, respectively.

Chapter 4

Analysis of K^+K^- production data

The measurement of the $pp \to ppK^+K^-$ reaction, being the subject of the present work, was performed in 2005 during one week of the COSY beam time. The measurement was carried out at the beam momentum equal to 3.316 GeV/*c*, corresponding to an excess energy in the ppK^+K^- system of 4.5 MeV. This chapter describes the data analysis for this channel and for the elastic proton-proton scattering which was used to determine the luminosity in the experiment.

4.1 Calibration of detectors

Analysis of the collected data for the $pp \to ppK^+K^-$ reaction was performed in a few steps. As a preparatory step calibration of detectors was performed. It included the space-time calibration of the drift chambers and the time calibration of the scintillation hodoscopes.

4.1.1 Calibration of drift chambers

In the drift chambers, the measurement of the drift time of the ionization electrons is used for determination of the track distance to the anode wire. This requires knowledge of the relationship between the distance d and the drift time t, referred to as the $d(t)$ relation. The determination of this function based on experimental data is called drift chamber calibration. In the present experiment the calibration was done individually for each detection plane of the drift chambers D1 and D2, containing altogether 6 + 8 = 14 planes.

Before the calibration time offsets of different drift cells, resulting, e.g. from differences in a length of the signal cables, were equalized based on the drift time spectra determined for the individual cells. Differences in the time offsets manifest themselves in the spectra as differences in the positions of the slopes corresponding to the vicinity of

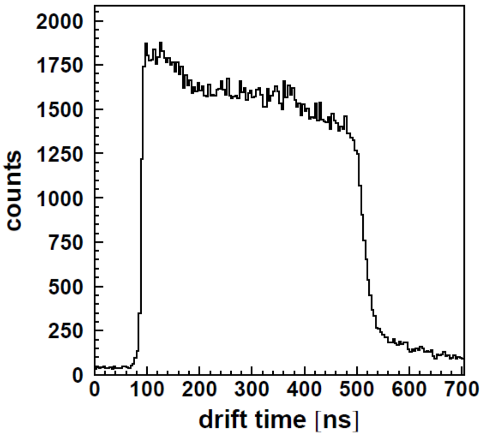

Figure 4.1: Drift time spectrum in a single drift cell. The left edge of the spectrum, at around 100 ns, corresponds to the vicinity of the anode wire. The right edge, at around 500 ns, corresponds to the maximum distance from the anode wire, which is equal to 2 cm.

the anode wire, which can be seen in Fig. 4.1. The time offsets of different drift cells were equalized by adding extra delays to the measured drift time, so that the positions of the slopes in the drift time spectra were the same for all cells.

The calibration of drift chambers was performed using an iterative procedure. The first iteration starts with an approximate $d(t)$ relation. It was usually taken from previous experimental runs. In principle it could also be determined for example by using the uniform irradiation method [41]. A correction to this relation is determined as a function of the drift time t_i corresponding to the TDC channel i. This correction is calculated as a mean deviation between the measured distance $d(t_i)$ of track to the anode wire corresponding to the drift time t_i and a distance $d^*(t_i)$ of the fitted track to the anode wire:

$$\Delta d(t_i) = < d(t_i) - d^*(t_i) >, \tag{4.1}$$

where the mean $< >$ is taken over all hits which were registered in the TDC channel i. The new calibration function, calculated as $d(t_i) - \Delta d(t_i)$, is an initial function for the next iteration. The iterative procedure is repeated until the corrections $\Delta d(t)$ become negligible in comparison to the spatial resolution of the chambers ($\sigma \sim 200\,\mu$m).

Left-hand side of Fig. 4.2 presents the time-space calibration function $d(t)$ of an arbitrarily chosen D1 plane. A distance from the anode wire varies approximately linearly with time in the interval from about 100 to 500 ns. The 100 ns corresponds to the proximity of the wire and is the value of the time offset introduced by the electronics. The right-hand side of Fig. 4.2 presents an example of the average deviation $\Delta d(t)$ between the fitted and measured distance of track from the sense wire as a function of the drift time.

The drift velocity of electrons in the drift chamber gas depends on its pressure. Due to

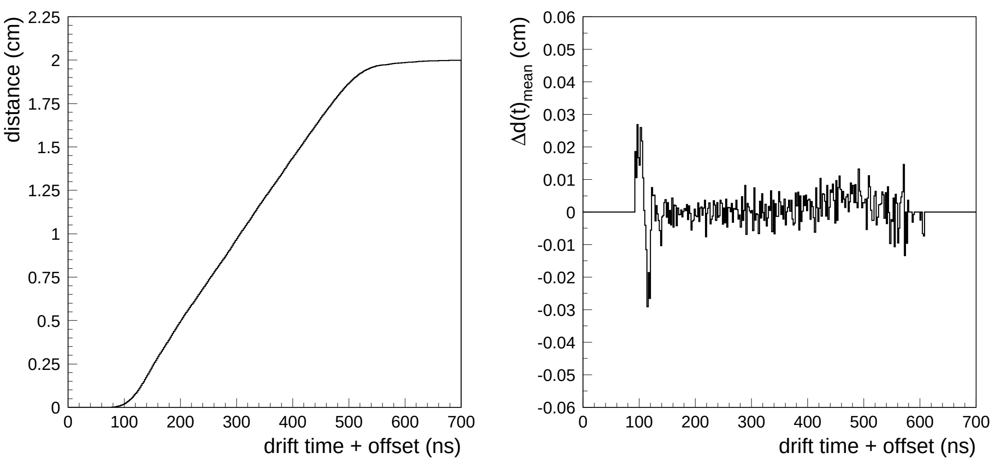

Figure 4.2: Time-space calibration for a single detection plane in the drift chamber D1 (left). The mean deviation between the measured and the fitted distance of track from the sense wire as a function of the drift time after the second iteration of the calibration procedure (right).

fluctuation of the atmospheric pressure, the drift velocity changes leading to variation of the chamber calibration. In order to account for this variation, the collected data were divided into measuring periods with a duration of a few hours and for each period a separate drift chamber calibration was performed.

4.1.2 Time-of-flight calibration

In the present experiment identification of positively charged reaction products (p, K^+ and π^+) is based on the ToF measurement using the S1, S2 and S3 hodoscopes. A precise calibration of these hodoscopes is crucial for a clean particle identification. The main element of the calibration is determination of the relative time offsets between the modules of the S1 and S2, as well as between the photomultipliers (PM) in the S3 scintillator wall.

For the S1 calibration, the fact that there is a 1 mm overlap between each two adjacent modules and that the charged particle crossing the overlap is registered in the both modules was used. A particle passing through both modules produces scintillation signals in them virtually at the same moment of time. The measured TDC values for the upper and lower photomultiplier in one S1 segment can be expressed as

$$TDC_{S1}^{up} = t_{S1} + \frac{y}{v} + t_{walk}^{up} + t_{offset}^{up} - t_{trigger}, \qquad (4.2)$$

$$TDC_{S1}^{down} = t_{S1} + \frac{L-y}{v} + t_{walk}^{down} + t_{offset}^{down} - t_{trigger}, \qquad (4.3)$$

where t_{S1} is the real time when the particle crosses the S1 detector; v is an effective velocity of the scintillation light propagation along the S1 segment; y is the distance between the hit position and the upper edge of the scintillator; L is a length of the S1 segment; t_{walk} is the time walk effect correction [38]; t_{offset} is the time offset of the electronics for a given photomultiplier; $t_{trigger}$ is the time when the trigger pulse starts the readout of TDC modules.

The time t_{S1}, corresponding to the moment when the particle crosses the S1 segment, is taken as the start time in the ToF measurements. According Eq. 4.2 and 4.3, t_{S1} can be expressed as:

$$t_{S1} = \frac{1}{2}(TDC_{S1}^{up} + TDC_{S1}^{down}) - \frac{L}{2v} - \frac{1}{2}(t_{walk}^{up} + t_{walk}^{down}) - \frac{1}{2}(t_{offset}^{up} + t_{offset}^{down}) + t_{trigger}. \quad (4.4)$$

The mean time offset of the upper and lower photomultiplier $t_{offset} = \frac{1}{2}(t_{offset}^{up} + t_{offset}^{down})$ is determined for each S1 segment in the calibration procedure.

At the beginning of the calibration procedure, the time offset for the first module in S1 is set arbitrarily. Next, the time difference between the 2nd module and the 1st module, measured with particles passing through both modules, is taken as a correction for the time offset of the second module. That procedure is repeated for all modules. Left-hand side of Fig. 4.3 presents the time difference between 6th and 7th module of the S1 after the calibration. The time difference is peaked around the zero which confirms the proper calibration of the S1 segments. The corrections for the time walk t_{walk}^{up} and t_{walk}^{down} are determined for each PM signal based on the signal amplitude measured with the ADC.

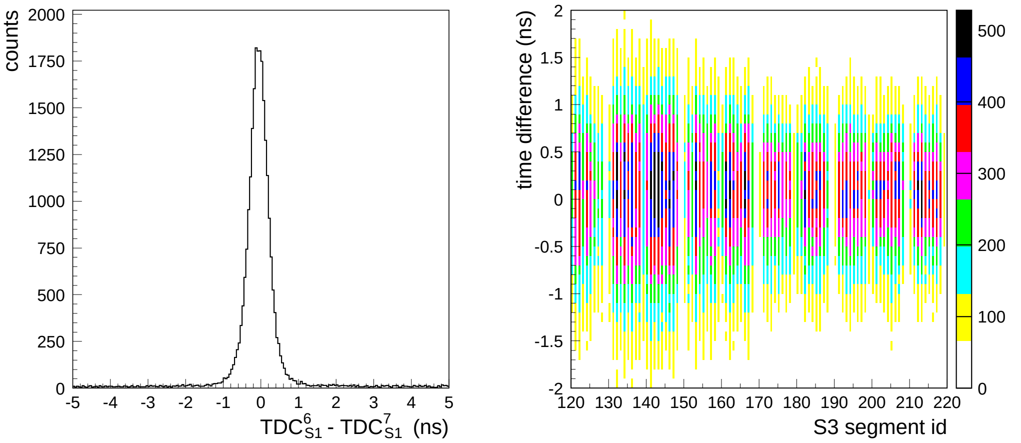

Figure 4.3: Time difference between 6th and 7th module of the S1 after the calibration (left). Difference between time of flight of protons, measured between S1 and S3 detectors and calculated from the reconstructed momentum, plotted for an arbitrarily chosen range of S3 segments (right).

Determination of the time offsets for the segments of the S2 hodoscope was performed using the S1 hodoscope as a reference detector. The offsets were adjusted in such a way that the time difference between the S1 and the S2 segment ($t_{\mathrm{S1}} - t_{\mathrm{S2}}$) was centered on zero.

The time calibration of the S3 photomultipliers was done after the correction of the time offsets in the S1 detector. That means that the start time for the time-of-flight measurement was known. Now, in order to determine the stop time, the time offsets for each of the 217 S3 photomultipliers were calculated. Analogously to the case of the S1 detector, the TDC value for the individual single photomultiplier in the S3 detector is:

$$TDC_{\mathrm{S3}} = t_{\mathrm{S3}} + t_{\mathrm{p}} + t^{\mathrm{S3}}_{\mathrm{walk}}(\mathrm{PM}) + t^{\mathrm{S3}}_{\mathrm{offset}}(\mathrm{PM}) - t_{\mathrm{trigger}}, \tag{4.5}$$

where t_{S3} is the time when the particle crosses the S3 scintillator; t_{p} is the time that light needs to pass from the scintillation origin to the photomultiplier photocathode; $t^{\mathrm{S3}}_{\mathrm{walk}}(\mathrm{PM})$ is the time walk effect correction; $t^{\mathrm{S3}}_{\mathrm{offset}}(\mathrm{PM})$ is the time offset of the electronics for a given photomultiplier. Because the value of t_{trigger} is the same for S1 and S3, and the correction for the time walk is calculated based on the measured amplitude of the PM signal, the value of time of flight depends only on the unknown time offset $t^{\mathrm{S3}}_{\mathrm{offset}}(\mathrm{PM})$. This offset can be calculated for each individual photomultiplier by comparing the ToF values measured with TDC and the same calculated from the momenta of particles reconstructed in the magnetic field. Only events with identified proton tracks were used in this calibration. The differences after the calibration for some arbitrarily chosen range of the S3 photomultipliers are presented in the right-hand side of Fig. 4.3.

4.2 Search for $\mathrm{K^+K^-}$ events

The main goal of the analysis of $\mathrm{K^+K^-}$ production data was to calculate the total cross section for the reaction $\mathrm{pp \to ppK^+K^-}$ at the beam momentum for which the measurement was performed. To do that one had to know:

- the number of registered events corresponding to the investigated reaction,
- the integrated luminosity,
- the detector efficiency and geometrical acceptance.

To achieve the first point, all products of the reaction must be identified. Identification of the positively charged reaction products (p, $\mathrm{K^+}$) is based on the momentum reconstruction combined with the time-of-flight determination.

4.2.1 Momentum reconstruction

The first step of the data analysis was the momentum reconstruction of the registered particles. For this the trajectories of particles registered in the drift chambers D1 and D2 (see Fig. 4.4) were reconstructed as sections of a straight line. Next, each reconstructed track was traced in the field of the COSY-11 dipole magnet using the available field maps and assuming a certain starting value of the particle momentum. For the track reconstructed in the magnetic field, a distance d between the track projection on the horizontal plane and the nominal target position was determined. In the next step the track reconstruction was repeated with corrected momentum of the particle, so as to obtain a value of the d significantly smaller than the size of the beam-target interaction area (∼10 mm). This procedure provided the absolute value of the particle momentum, the components x, y, z of the momentum at the interaction point, as well as the distance of the reconstructed track from the nominal target position in the vertical direction. Figure 4.5 presents distribution of the reconstructed vertical position of the particle track at the target for the simulation and the experimental data. Red lines present a cut made in order to suppress events originating from the beam interaction with the residual target gas and from scattering of the produced particles on the dipole magnet pole shoe.

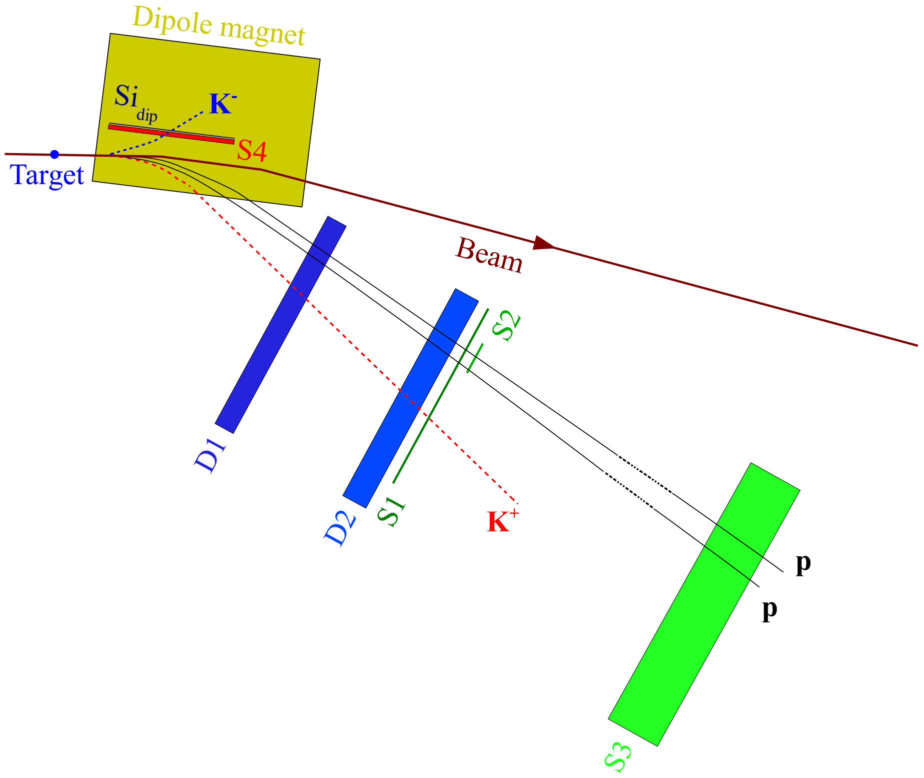

Figure 4.4: Principle of the $pp \to ppK^+K^-$ measurement with the COSY-11 detection system.

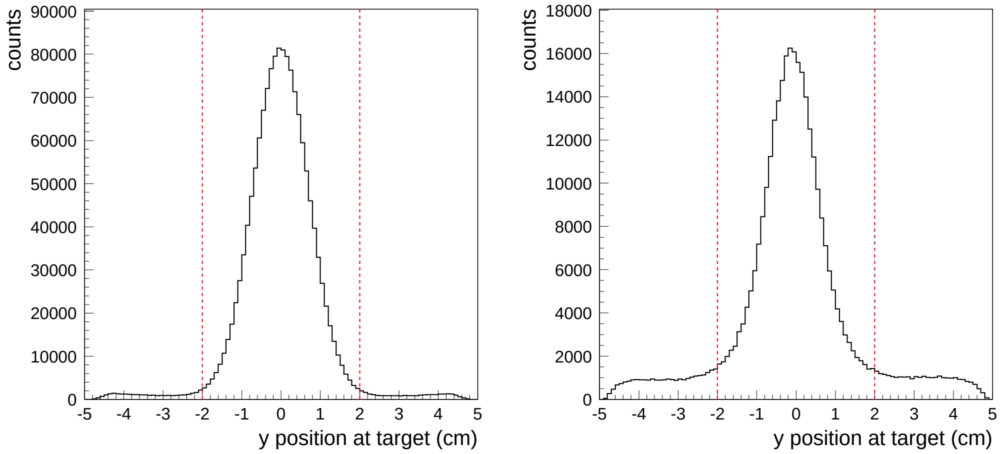

Figure 4.5: Vertical position at the target of the reconstructed track for simulation (left) and experimental data (right). The accepted range of the position is indicated with the vertical dashed lines.

4.2.2 Identification of protons

The next step in the data analysis was identification of protons. It was based on the time of flight between S1 and S3. Only tracks reconstructed in D1 and D2 passing through segments in S1 which produced signals and pointing towards S3 were taken into account. In addition it was required that the distance of the track to the nearest cluster in S3 was less than 15 cm (see Fig. 4.6).

To identify the particle its invariant mass was calculated according the formula:

$$m_{\text{inv}} = p\sqrt{\frac{1-\beta^2}{\beta^2}}, \tag{4.6}$$

where p is the reconstructed momentum; β is particle velocity, expressed relative to the speed of light c, determined from the time of flight between S1 and S3 and the known path between S1 and S3. Figure 4.7 presents simulated and measured invariant mass for particles registered in S1 and S3. Condition chosen for the proton identification is marked on the experimental spectrum by two dotted red lines including the proton peak. Only events with identified two protons were taken for further analysis.

4.2.3 Identification of K^+ mesons

In contrast to the outgoing protons, the positively charged kaons from the measured reaction are not registered in the S3 hodoscope due to the approximately two times smaller

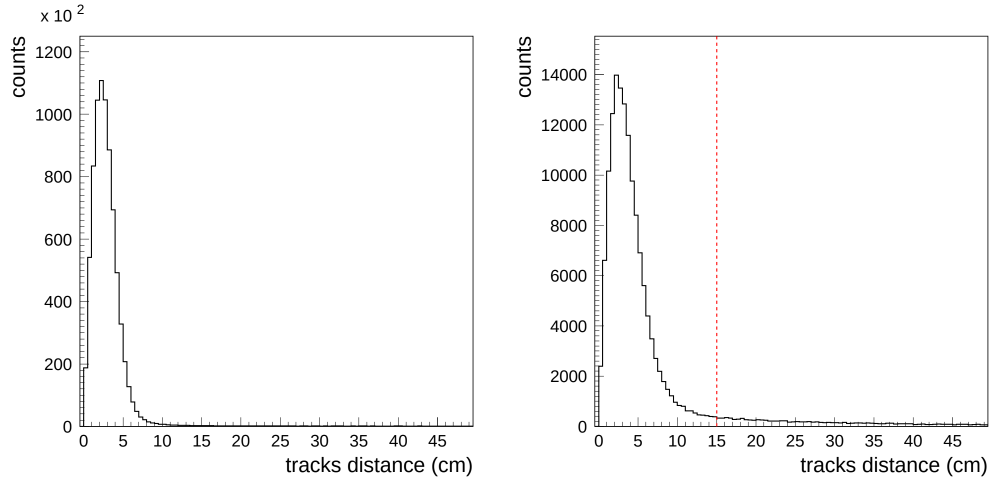

Figure 4.6: Simulated (left) and measured (right) distance between reconstructed track and S3 cluster. Red line presents selected upper limit of the distance for accepted tracks.

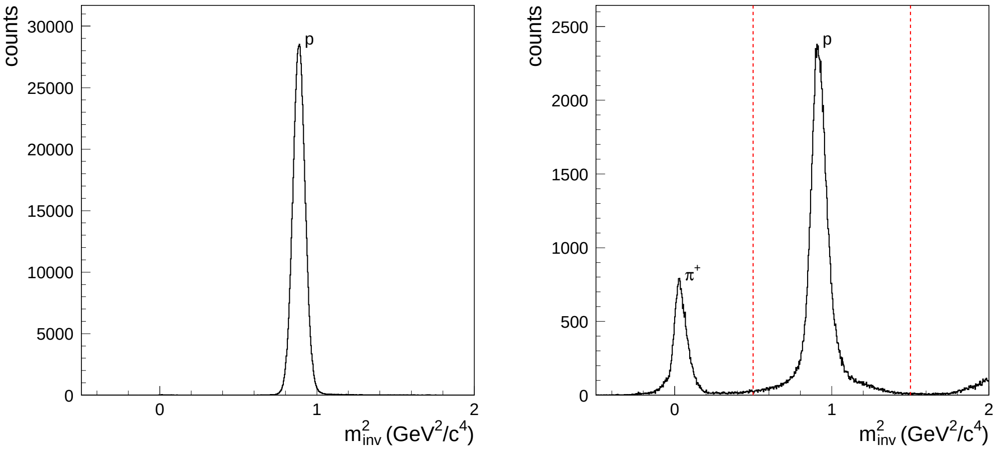

Figure 4.7: Simulated (left) and measured (right) invariant mass squared of particles registered in S1 and S3. Red lines present selected range for protons identification.

momentum than that of the protons and respectively two times larger deflection of their trajectories in the field of the dipole magnet. Besides, due to their finite life time equal to about 12 ns, most of them decay on a path of a few metres.

Therefore to identify them their time of flight on the path between the target and the S1 hodoscope (about 3 m) was used. For this the moment of the reaction in the target (reaction time) was determined as the mean value of the reaction times calculated for each of the two protons:

$$t_{\text{target}} = \frac{t_{\text{start}}^{(p_1)} + t_{\text{start}}^{(p_2)}}{2}. \tag{4.7}$$

There are two possible scenarios for the registration of the two protons in S1. In the first scenario, each proton passes through a different S1 segment, which is presented in the left-hand side of Fig. 4.8. The reaction time for each proton ($t_{\text{start}}^{(p_1)}$ and $t_{\text{start}}^{(p_2)}$) is calculated using the path l between the target and S1, hit time t_{S1} and the velocity of the proton β_p:

$$t_{\text{start}} = t_{S1} - \frac{l}{\beta_p c}, \tag{4.8}$$

where β_p is determined based on the measured momentum of the proton and its mass:

$$\beta_p = \frac{p}{\sqrt{p^2 + m_p^2 c^2}}. \tag{4.9}$$

In the second scenario (right-hand side of Fig. 4.8), both protons pass through the same S1 segment, but two different S2 segments. In this case the reaction time for each proton is calculated using the time information from the S2 detector:

$$t_{\text{start}} = t_{S2} - \frac{l}{\beta_p c}. \tag{4.10}$$

The reaction time resolution for protons registered in S1 or S2 is determined based on the difference of the times for the two protons from the same event:

$$\Delta t_{\text{start}} = t_{\text{start}}^{(p_1)} - t_{\text{start}}^{(p_2)}. \tag{4.11}$$

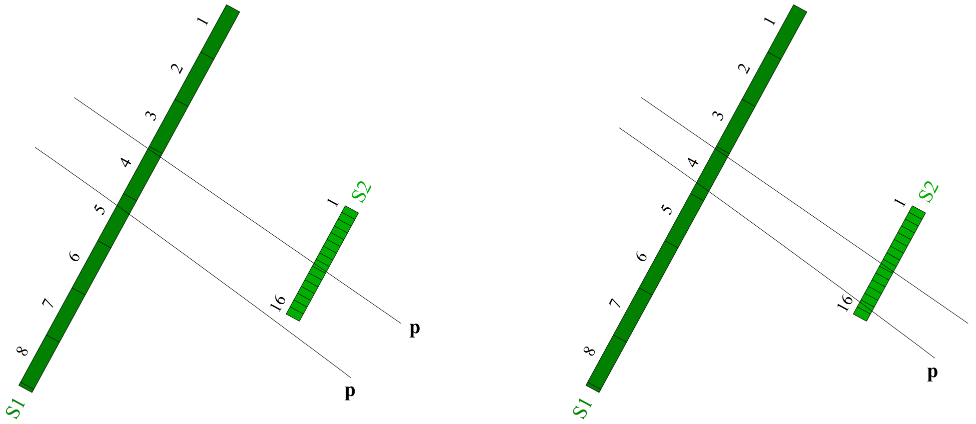

Figure 4.8: Two-proton measurement scenario with both protons registered in two different S1 segments (left) and with both protons registered in the same S1 segment but two different S2 segments (right).

It is presented in the left and right part of Fig. 4.9 for simulated and measured events respectively. In order to reduce the background coming from reactions on the rest gas in the beam line and from pions misidentified as protons, events outside the region marked by two red lines were rejected.

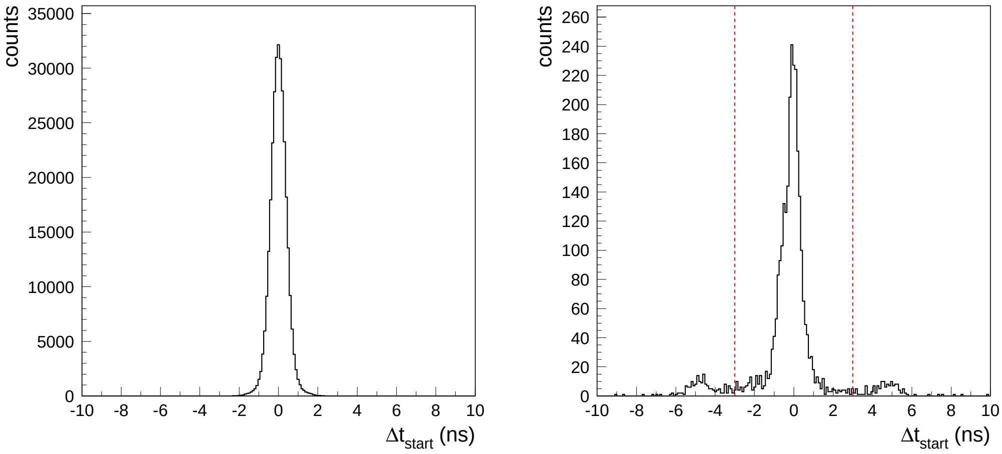

Figure 4.9: Simulated (left) and measured (right) reaction times difference calculated for two identified protons. The two small peaks, visible in the experimental spectrum on the left and right side of the main peak, come from pions erroneously identified as protons. Only events in the range indicated by the two red lines were selected.

Knowing the reaction time, the invariant mass of the positively charged particle going through S1 and associated with the two protons was calculated using Eq. 4.6, with β calculated as:

$$\beta = \frac{l}{tc}, \tag{4.12}$$

where l is the particle path and t equals:

$$t = t_{S1} - t_{\mathrm{target}}. \tag{4.13}$$

Top part of Fig. 4.10 presents the invariant mass spectra of the third positively charged particle from the simulations and the experiment. The simulations were done for the studied reaction and for the pion production background reactions. In the invariant mass spectrum from the simulations, the pion peak is clearly separated from the kaon peak. The former dominates the experimental spectrum and at the kaon mass there is a slight increase, but not significantly above the background.

The next step of the data analysis was taking into account the fact that, according to the simulations, the positive kaons from the $pp \to ppK^+K^-$ reaction are registered in S1 segments from 9 to 12 (see bottom left-hand side of Fig. 4.10). In the bottom right-hand side of Fig. 4.10, the measured invariant mass spectrum of the third particle registered in

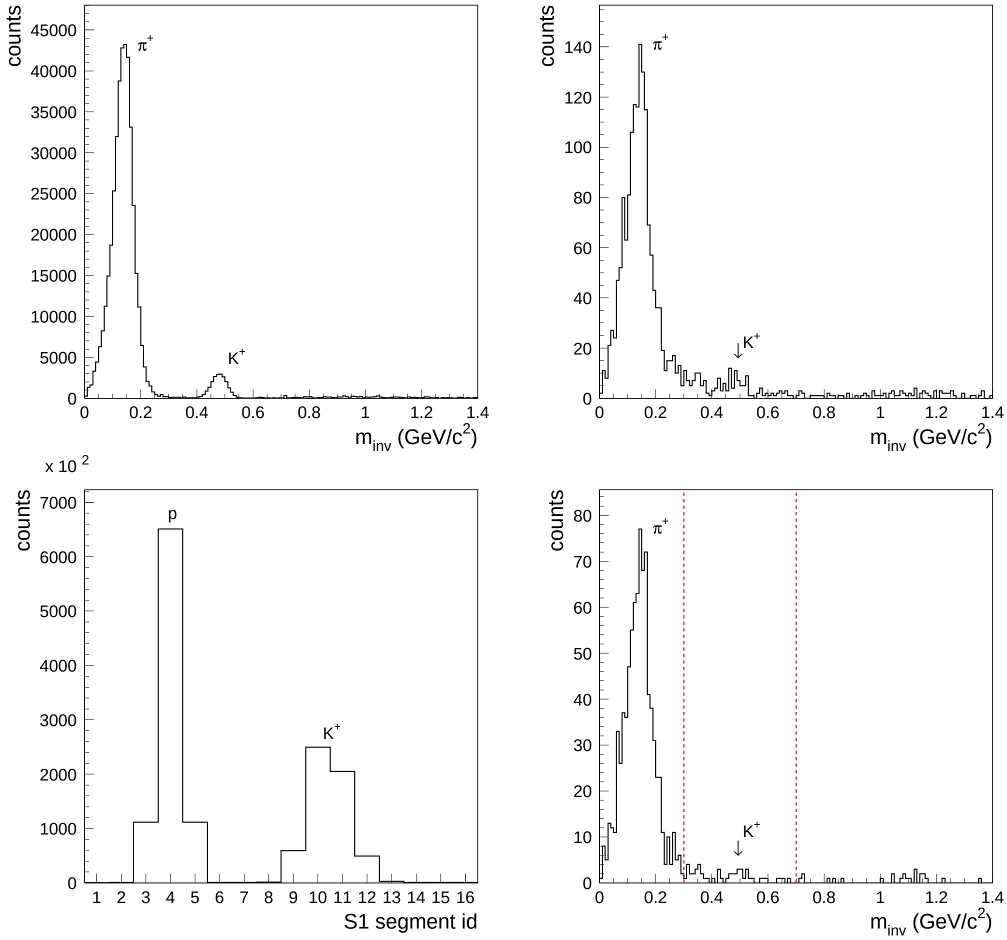

Figure 4.10: TOP: Simulated (left) and measured (right) invariant mass spectra of the third (non-proton) particle registered in S1. In the simulation only the investigated reaction and one of the background pion production reactions ($pp \rightarrow pp\pi^+\pi^-$) are included. BOTTOM: Distribution of counts in S1 segments for p and K^+ from $pp \rightarrow ppK^+K^-$ reaction obtained in simulation (left) and measured invariant mass of the third (non-proton) particle registered in S1 with condition that one particle is registered in S1 segments from 9 to 12 (right). Red lines present selected condition for the K^+ identification.

the S1, after taking into account that additional requirement, is presented. In K^+ identification region, selected as shown by the red lines, the spectrum is dominated by the tail from the pion peak and there is no significant signal at the kaon mass.

4.2.4 Selection of $pp \rightarrow ppK^+K^-$ events

After the identification of the all three positively charged particles, the missing mass of the ppK^+ system was calculated:

$$m_{\mathrm{miss}} = \sqrt{(E - \sum_{i=1}^{3} E_i)^2 - (\sum_{i=1}^{3} p_{x_i})^2 - (\sum_{i=1}^{3} p_{y_i})^2 - (p_{\mathrm{beam}} - \sum_{i=1}^{3} p_{z_i})^2}. \qquad (4.14)$$

That value should correspond to the K^- mass. Spectra of the missing mass squared from the simulation and experiment are presented in Fig. 4.11.

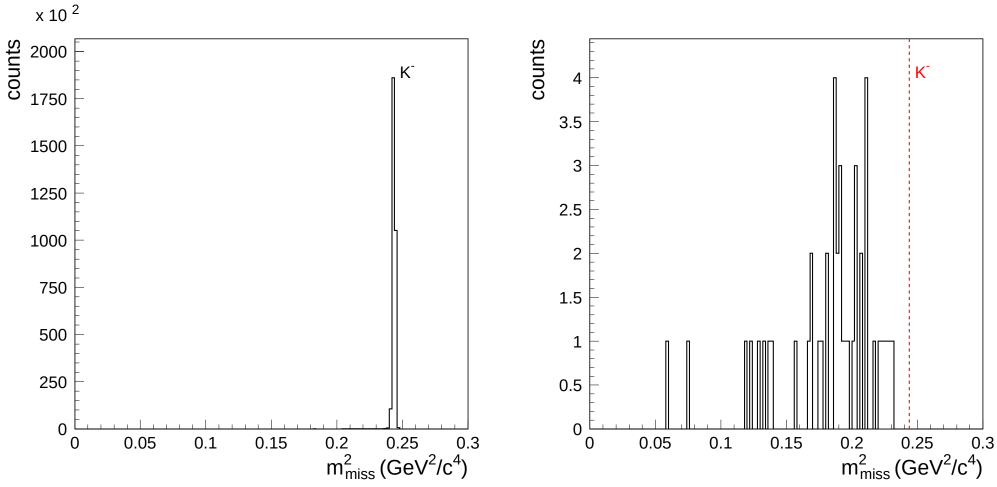

Figure 4.11: Simulated (left) and measured (right) missing mass squared of the ppK^+ system.

As one can see, there is no expected signal from the negatively charged kaons on the experimental plot. This is much more visible on the two-dimensional plot, presenting invariant mass squared of the third positively charged particle registered in the S1 detector besides the two protons, as a function of the missing mass squared of the ppK^+ system, shown in the top part of Fig. 4.12. In the figure the plot is presented both for simulations and for measurements together with the 3σ limits of the probability distribution for the observation of the K^+ meson. No events are observed within these limits in the experimental plot. That means that there are no events from the $pp \rightarrow ppK^+K^-$ reaction observed.

Events outside the region of interest come from background reactions. Monte Carlo simulations of the most obvious background reactions were performed and the summary of the simulation results is presented in the bottom part of Fig. 4.12.

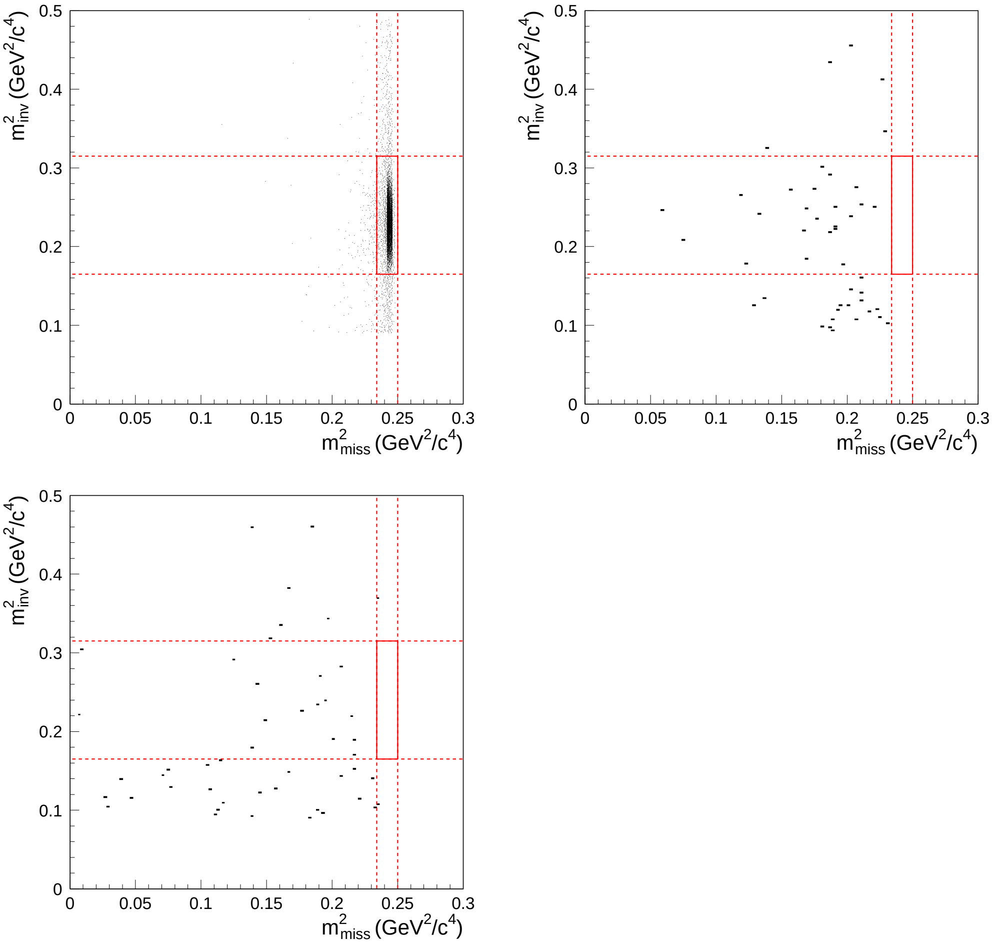

Figure 4.12: TOP: Simulated (left) and measured (right) two-dimensional plot of invariant mass squared of the third (non-proton) particle squared versus missing mass of the ppK^+ system. Red lines present region where signal from ppK^+K^- reaction is expected. BOTTOM: Simulated events from the reactions used for background estimation. Red lines present the 3σ region where signal from the ppK^+K^- reaction is expected.

The main contributions to the background come from reactions of the type $pp \to pK^+X$. Expected number of background events was estimated using corresponding total cross sections, the integrated luminosity in the measurement and COSY-11 acceptance. Results of those calculations are given in the Tab. 4.1. The discrepancy between the simulated and measured number of background events (61 and 85 respectively) can come from not included in the calculation the $pp \to pK^+\Lambda(1405)$ reaction, with the $\Lambda(1405)$ hyperon decaying into a $\Sigma\pi$ pair and the Σ decaying into a $N\pi$ pair. Published experimental data for that reaction [42] are not sufficient to extrapolate the total cross section to the present energy. Another difficulty is caused by the fact that the current energy lies below the threshold for that reaction and only because of the finite width of the $\Lambda(1405)$ of Γ = 50 MeV, the low energy tail of the hyperon leads to the production of events above threshold.

Reaction	**Q (MeV)**	**σ (μb)**	**Events**
$pp \to pK^+\Sigma(1385)^0$	53	0.4	28
$pp \to pK^+\Sigma^0$	244	10	0
$pp \to pp\pi^0 2\pi^+ 2\pi^-$	299	80	10
$pp \to pp3\pi^0\pi^+\pi^-$	308	80	4
$pp \to pK^+\Lambda$	321	40	0
$pp \to pp2\pi^+2\pi^-$	433.5	200	10
$pp \to pp2\pi^0\pi^+\pi^-$	443	50	1
$pp \to pp\pi^0\pi^+\pi^-$	578	700	6
$pp \to pp3\pi^0$	587	1000	0
$pp \to pp\pi^+\pi^-$	712	2670	2
$pp \to pp2\pi^0$	722	1000	0
$pp \to pp\pi^0$	857	3850	0
Total from simulation		**61 events**	
Total from experiment		**85 events**	

Table 4.1: Reactions used for background estimation with their excess energy, total cross section values (for that energy) [42–44] and expected number of events with the integrated luminosity experimental value calculated in the next section and the acceptance given by the simulation.

4.3 Integrated luminosity

The total cross section σ_{tot} for the studied reaction was determined using the standard formula:

$$\sigma_{\mathrm{tot}} = \frac{N}{\varepsilon}\mathcal{L}, \tag{4.15}$$

where N is the number of registered events, ε is the detector acceptance and $\mathcal{L}$ is the luminosity L integrated over the measuring time:

$$\mathcal{L} = \int L\,\mathrm{d}t. \tag{4.16}$$

In the experiment the luminosity was monitored using a coincidence measurement of the elastically scattered protons. A principle of the measurement of the proton-proton elastic scattering is explained in Fig. 4.13. Proton scattered in the forward direction is bent in the magnetic field of the dipole magnet and is registered in the drift chambers D1, D2 and in the scintillation hodoscope S1. This allows the reconstruction of the proton's momentum vector at the target. The recoil proton is detected in the scintillation detector S5 and in the position sensitive silicon pad detector $\mathrm{Si}_{\mathrm{mon}}$, allowing the determination of the scattering angle θ_2 of the proton.

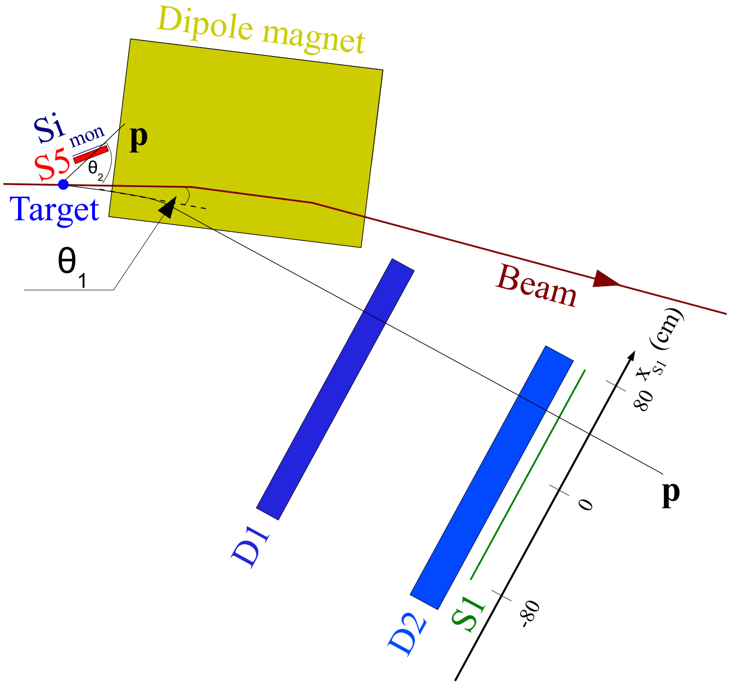

Figure 4.13: Principle of the proton-proton elastic scattering measurement with the COSY-11 detection system.

In the first step of selection of the proton-proton elastic scattering events, a threshold was set for amplitude of the $\mathrm{Si}_{\mathrm{mon}}$ signals in order to suppress electronic noise. A level of the threshold was set by comparing amplitude spectra from silicon pads where only noise is expected with ones where also signal from the recoil protons is expected, according the Monte Carlo simulations. Examples of the amplitude spectra for pads with and without the protons signal are presented in Fig. 4.14. The selected threshold is also indicated.

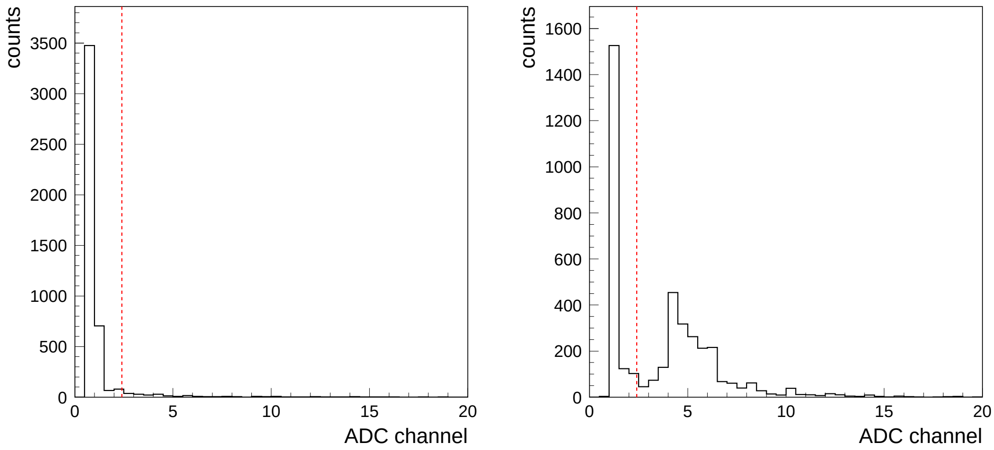

Figure 4.14: Amplitude spectrum of $\mathrm{Si}_{\mathrm{mon}}$ detector pad containing only entries from the electronic noise (left) and a spectrum comprising also a signal from the elastically scattered protons (right). Red lines present chosen threshold for noise rejection.

The elastic scattering two-body kinematics requires that the parallel (p_{L}) and perpendicular (p_{T}) components of the momentum vector of the scattered proton form an ellipse (see Fig. 4.15). In the second step of selection of the elastic scattering events, the distance to the theoretical kinematical ellipse was used to reject some part of events from background reactions. A 4σ cut was applied to the distribution of the distance in order to suppress the background events (see Fig. 4.16).

The last condition used for selecting the proton-proton elastic scattering was based on the fact that the scattering angles θ_1 and θ_2 of the forward scattered and recoil protons are kinematically connected. This manifests in correlation between the coordinates of their tracks measured at the position of the S1 and $\mathrm{Si}_{\mathrm{mon}}$ detector respectively (see Fig. 4.17). In order to exploit this correlation, the angular range covered by the S1 detector, θ_1^{cm} between 42° and 64°, was divided into eleven intervals with a width of $\Delta\theta_1^{\mathrm{cm}} = 2°$. For each interval a projection of the data points from Fig. 4.17 lying along the expected correlation line on an axis perpendicular to the correlation line was determined. An example projection is shown in Fig. 4.18. Elastic events are visible as a peak over a background which comes from the pion(-s) production reactions. A linear fit was used for the background subtraction. A percentage of the background events lying under the elastic peak, for the selected angular intervals, ranges from 0.38% to 4.59%. Uncertainty of the number of elastic events associated with the background subtraction was estimated using two different models of the background shape: linear and constant one. This uncertainty amounts to less than 0.2%.

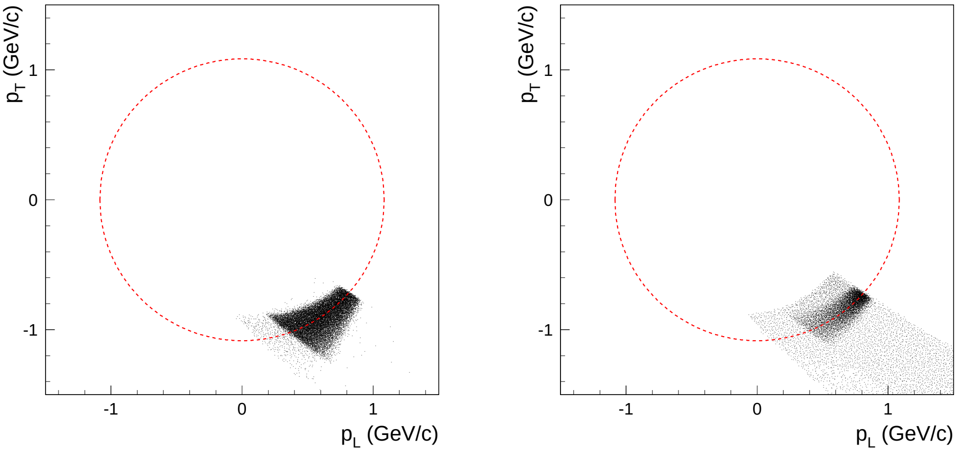

Figure 4.15: Simulated (left) and measured (right) distribution in the centre of mass system of transverse versus longitudinal momentum of the forward scattered protons from the proton-proton elastic scattering.

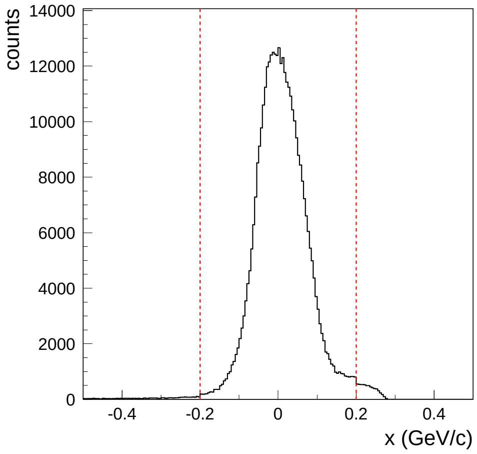

Figure 4.16: Distribution of the elastic proton-proton events in function of the distance to the kinematical ellipse. Red lines present the applied 4σ cut.

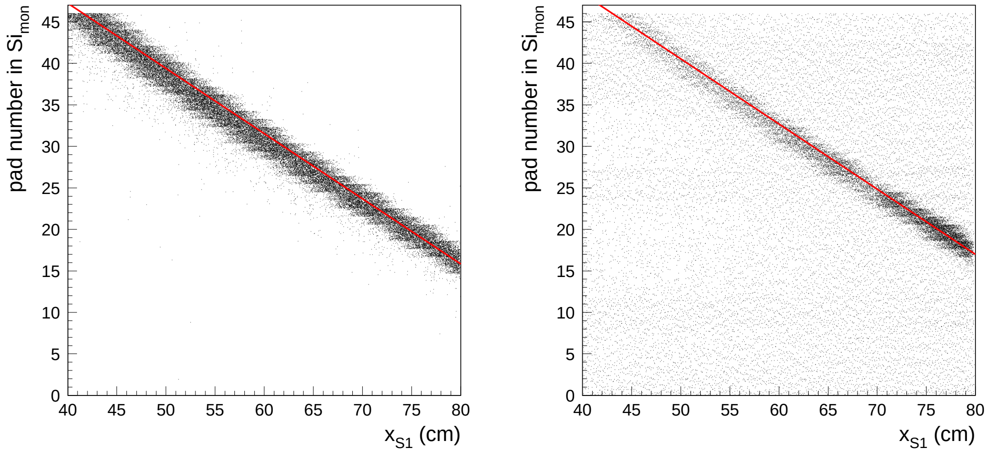

Figure 4.17: Simulated (left) and measured (right) correlation between the position in the $\mathrm{Si_{mon}}$ and the S1 detectors for the elastically scattered protons. Red lines present correlation calculated according the two-body kinematics of the proton-proton elastic scattering.

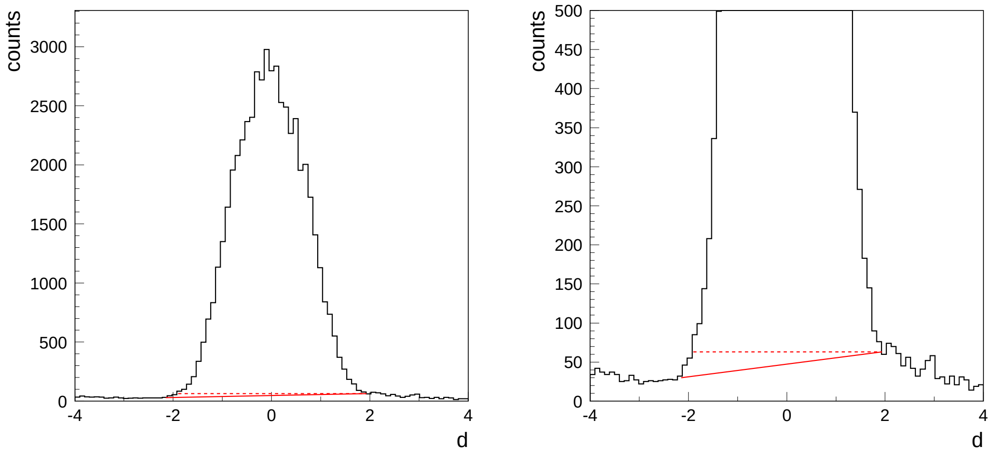

Figure 4.18: Distribution of events as a function of the distance to the theoretical correlation function (red line on Fig. 4.17) with two different (solid and dotted lines) background estimation functions (left). The same distribution but with a reduced range of the y-axis for a better presentation of the background (right).

The number of entries in the observed peak, after the background subtraction, gives the number of events $\Delta N_{pp}(\theta_1^{cm})$ of protons scattered in a given polar angle interval $\Delta\theta_1^{cm}$. Solid angle $\Delta\Omega^{cm}$ covered by the detection system and corresponding to the $\Delta\theta_1^{cm}$ interval was determined using the Monte Carlo technique and was calculated using the formula

$$\Delta\Omega^{\mathrm{cm}} = 4\pi \frac{N_{\mathrm{r}}}{2N_{\mathrm{s}}}, \tag{4.17}$$

where 4π corresponds to the full solid angle; N_{r} is the number of the registered protons in a given S1 region; factor 2 in the denominator results from two indistinguishable protons which are elastically scattered; N_{s} is the number of the simulated events of the elastic scattering. The integrated luminosity was determined independently for each interval of the polar angle θ_1^{cm} using the formula

$$\mathcal{L} = P \frac{\Delta N_{\mathrm{pp}}(\theta_1^{\mathrm{cm}})}{\Delta\Omega^{\mathrm{cm}}(\theta_1^{\mathrm{cm}}) \frac{d\sigma}{d\Omega^{\mathrm{cm}}}(\theta_1^{\mathrm{cm}})}, \tag{4.18}$$

where $P = 2^6$ is a prescale factor applied in the triggering electronics for the elastic events and $\frac{d\sigma}{d\Omega^{\mathrm{cm}}}$ is the differential cross section for the proton-proton elastic scattering. Numerical values of the elastic cross sections were taken from the high precision measurements performed by the EDDA collaboration [45]. The angular distribution of the differential cross sections from EDDA and from present measurement is shown in Fig. 4.19.

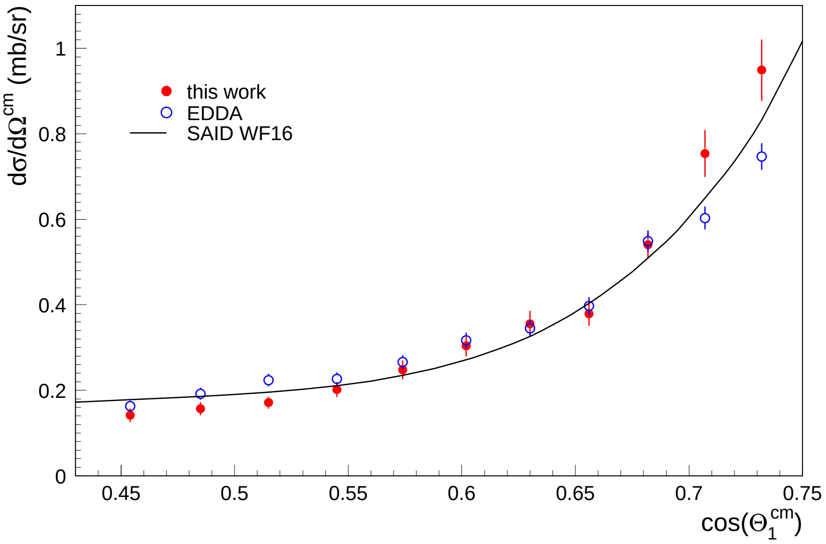

Figure 4.19: Angular distribution of the differential cross section for the proton-proton elastic scattering obtained in the current measurement (full dots) compared to the data from the EDDA experiment [45] (empty dots). The current data points were normalized using the integrated luminosity determined as an average of luminosities calculated independently for each of 11 polar angle θ_1^{cm} intervals. The solid line represents the cross section calculated with the partial-wave analysis code SAID, solution WF16 [46].

One can see in the figure that there is a discrepancy between the differential cross sections from these two data sets for the highest $\cos(\theta_1^{cm})$ values. Also cross section for the pp elastic scattering calculated with the partial-wave analysis code SAID, solution WF16 [46], well agrees with the current results and with the EDDA data, except points for the two highest $\cos(\theta_1^{cm})$ values. For these two values the SAID line lies between the present points and the EDDA points. Because of these discrepancies two data points with the highest $\cos(\theta_1^{cm})$ values have been removed from the luminosity calculations.

The integrated luminosity in the present experiment was determined as an average of the values calculated for individual polar angle intervals. Numerical values for each interval and the average luminosity are given in Tab. 4.2.

θ_1^{cm} (°)	ΔN_{pp}	$\Delta\Omega^{cm}$ **(msr)**	$\frac{d\sigma}{d\Omega^{cm}}$ **(mb/sr)**	$\mathcal{L}$ **(pb^{-1})**
47 ± 1	33 119	2.38	0.55 ± 0.02	1.62 ± 0.06
49 ± 1	24 223	2.49	0.4 ± 0.02	1.57 ± 0.07
51 ± 1	24 981	2.73	0.35 ± 0.02	1.7 ± 0.08
53 ± 1	23 175	2.96	0.32 ± 0.02	1.58 ± 0.08
55 ± 1	19 494	3.06	0.27 ± 0.01	1.54 ± 0.08
57 ± 1	16 870	3.25	0.23 ± 0.01	1.46 ± 0.08
59 ± 1	14 705	3.34	0.22 ± 0.01	1.26 ± 0.08
61 ± 1	12 385	3.06	0.19 ± 0.01	1.35 ± 0.09
63 ± 1	8 549	2.34	0.16 ± 0.01	1.44 ± 0.11
Average $\mathcal{L}$				**1.52 ± 0.03 pb^{-1}**

Table 4.2: Data used to derive integrated luminosity $\mathcal{L}$ for each individual angular interval and extracted average value of the luminosity.

The extracted average integrated luminosity amounts to $\mathbf{\mathcal{L} = 1.52 \pm 0.03_{stat} \pm 0.07_{syst}\ pb^{-1}}$. The indicated systematic uncertainty corresponds to precision of the normalization of the EDDA cross sections (2.5%) and systematic error of the solid angle ($\Delta\Omega^{cm}$) determination (2%). The systematic uncertainty originating from the background subtraction is less than 0.2% and is negligible. An average luminosity, calculated taking into account the total data taking time of 136 hours, is equal to $3.11 \pm 0.06\ \mu b^{-1}s^{-1}$.

4.4 Upper limit on the $\mathrm{pp} \to \mathrm{ppK^+K^-}$ total cross section

In order to calculate the total cross section for the studied reaction, according to the formula 4.15, besides the number of events and the integrated luminosity, also the acceptance of the detection system has to be known. The detector acceptance was determined using Monte Carlo simulations of the measurement of the $\mathrm{pp} \to \mathrm{ppK^+K^-}$ reaction. The $\mathrm{ppK^+K^-}$ events were generated according uniform distribution of the reaction products over the available phase space volume.

The pp FSI, which is very strong at low values of the relative momentum, was taken into account in the simulations by introducing for each event a weight equal to the enhancement factor [47] of the reaction amplitude due to the pp FSI. The enhancement factor was calculated in the finite range approximation with the Coulomb interaction included.

In the performed simulation, $1.2 \cdot 10^6$ events were generated. The finite lifetime of the produced charged kaons was taken into account. The MC events were analysed in the same way as the experimental data. The detector acceptance was determined as a sum of weights of events accepted in the analysis as $\mathrm{ppK^+K^-}$ events, divided by the sum of weights of all generated events. This acceptance is equal to **2.83%**. For comparison, the detector acceptance calculated with neglected pp FSI (i.e. by taking a ratio of numbers of accepted and generated events) equals 3.01%.

Since no $\mathrm{ppK^+K^-}$ events were observed in the experiment, only upper limit on the $\mathrm{pp} \to \mathrm{ppK^+K^-}$ total cross section could be determined. Because there was no background in the region of interest and integrated luminosity was fixed, the events follow a Poisson distribution [12]. With no observed events an upper limit for a Poisson variable at a confidence level (CL) of 95% is equal to 3.0 (see Tab. 4.3).

	1 - α = 90%		**1 - α = 95%**	
n	μ_{lo}	μ_{up}	μ_{lo}	μ_{up}
0	-	2.30	-	**3.0**
1	0.105	3.89	0.051	4.74
2	0.532	5.32	0.355	6.30
3	1.10	6.68	0.818	7.75
4	1.74	7.99	1.37	9.15
5	2.43	9.27	1.97	10.51

Table 4.3: Lower and upper (one-sided) limits for the mean μ of Poisson variable given n observed events in the absence of background, for confidence levels of 90% and 95%. Table adopted from Ref. [12].

The total cross section corresponding to three events, calculated using the integrated luminosity and the detector acceptance determined in the previous sections, is equal to **0.070 nb**. This value has to be understood as an upper limit at CL = 95% on the total cross section for the $pp \to ppK^+K^-$ reaction at the excess energy of 4.5 MeV. Table 4.4 presents values used in the calculations and the determined result.

Acceptance	2.83%
Integrated luminosity	1.52 pb^{-1}
Number of events at CL = 95%	3
Upper limit at CL = 95% on the total cross section	**0.070 nb**

Table 4.4: Obtained upper limit on the total cross section and values used for its calculation.

The momentum of the proton beam (3.316 GeV/c), calculated from the frequency of the COSY accelerator and the beam orbit length, is known with the precision of $\frac{\Delta p}{p} = 10^{-3}$ ($\Delta p = 0.003$ GeV/c). The corresponding uncertainty of the excess energy (4.5 MeV) is 1.2 MeV.

4.5 Discussion of results

The upper limit on the $pp \to ppK^+K^-$ total cross section at $Q = 4.5$ MeV, calculated using the obtained integrated luminosity and the acceptance, is presented in Fig. 4.20 together with other existing experimental data. The four curves shown in the figure present calculations of the total cross section versus energy including the final-state interactions between pp, pK^- and K^+K^- as described in the Section 2.4.

The solid curve, presenting the calculation with all included interactions, describes well the data points from previous experiments, but lies above the present upper limit: the limit is about three times smaller than the corresponding value of the calculation. This discrepancy can result from the Coulomb interaction between the final-state particles, which was not fully included in the calculations. It may also be due to the strong absorption of the kaons pair due to formation of the $K\bar{K}$ molecule. In this case, the strong K^+K^- interaction in the final state leads to the emergence of the molecule, which then decays into $\pi\pi$ pair with $I = 0$ or $\pi\eta$ pair with $I = 1$ (see Section 2.1).

In Ref. [48] the $pp \to ppK^+K^-$ reaction below the φ meson production threshold was studied within the effective Lagrangian approach. The authors assumed that the K^+K^- pair is produced through an intermediate state Λ, excited by the exchange of a pion between the protons: $pp \to pK^+(\Lambda \to pK^-)$ where Λ is either the off-shell $\Lambda(1115)$ or the subthreshold $\Lambda(1405)$. The FSI between outgoing protons was included using the Jost function (see Section 2.4) and the K^+K^- FSI was calculated in the framework of the chiral unitary approach, as in Ref. [49].

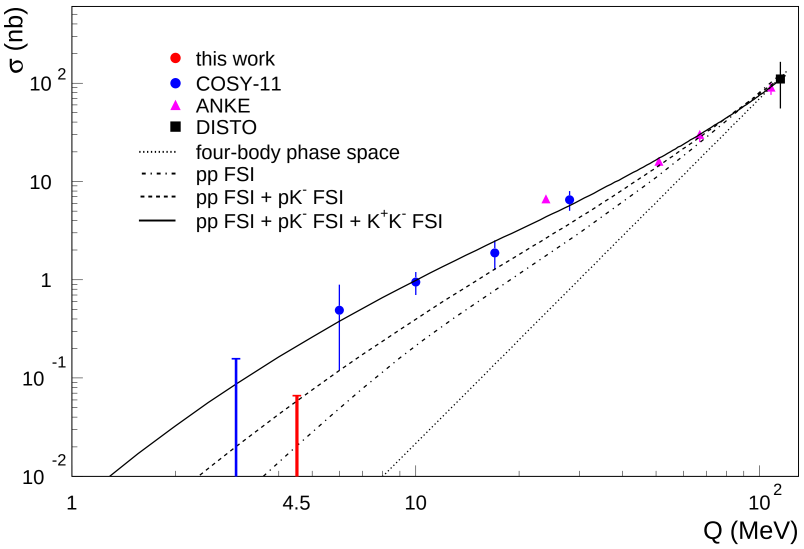

Figure 4.20: The $pp \to ppK^+K^-$ total cross section measured in previous experiments [7–11,24] together with the present upper limit at $Q = 4.5$ MeV and theoretical curves from Ref. [28] describing the FSI as presented in the text.

Calculations of the $pp \to ppK^+K^-$ total cross section were performed for four different sets of parameters of the model, including the type of πNN and KNΛ couplings (pseudoscalar or pseudovector), the parameters α and β in the Jost function and cut-off parameter for the exchanged pion. All four sets are listed in Tab. 4.5.

Set	πNN and KNΛ couplings	pp FSI (MeV)	Cut off (GeV)
I	PS	α = 19.7; β = 98.7	1.5
II	PS	α = -20.5; β = 166.7	1.3
III	PV	α = 19.7; β = 98.7	1.5
IV	PV	α = -20.5; β = 166.7	1.3

Table 4.5: Four different sets of parameters used in the description of the $pp \to ppK^+K^-$ reaction based on the effective Lagrangian approach [48].

The corresponding four theoretical dependencies of the total cross section on energy are compared with the experimental data in Fig. 4.21. They describe the previous data rather well. However, it should be noted that they lie above the current upper limit on the total cross section.

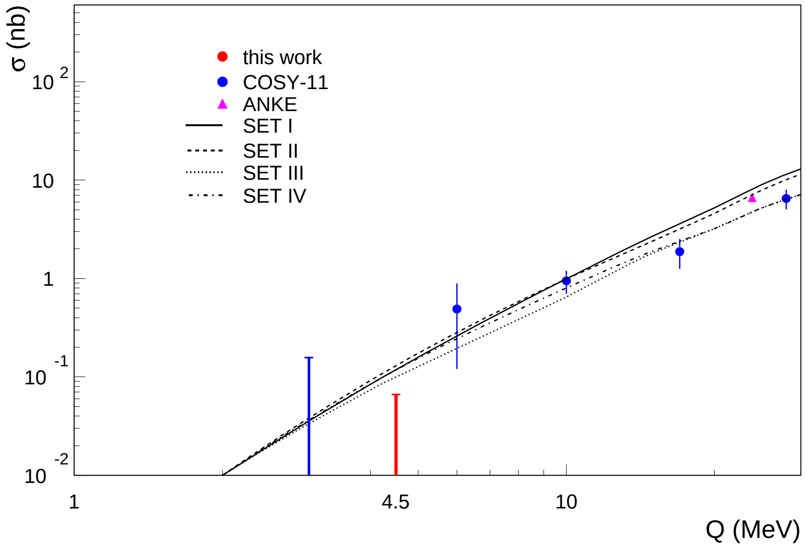

Figure 4.21: Data points for the $pp \to ppK^+K^-$ total cross section including the present upper limit at $Q = 4.5$ MeV. The lines present results of the theoretical studies within the effective Lagrangian approach, as described in the text.

Chapter 5

Analysis of $\mathrm{pp} \to \mathrm{ppX}$ events

The hardware trigger applied in the $\mathrm{pp} \to \mathrm{ppK^+K^-}$ measurements was general enough to also record events of the type $\mathrm{pp} \to \mathrm{ppX}$ (see Section 3.3). In the current chapter, the analysis performed of registered events of this type is described and results obtained for the $\mathrm{pp} \to \mathrm{pp}\omega$ and $\mathrm{pp} \to \mathrm{pp}\eta$' cross sections are presented. These results are of interest in the study of the ω and η' meson production in the proton-proton collisions, on the one hand. On the other hand, the value of the integrated luminosity obtained from the analysis of the proton-proton elastic scattering was validated by using them.

5.1 Missing-mass spectrum of the two-proton system

The data collected in the present experiment were also used for studies of the production of single mesons in the process $\mathrm{pp} \to \mathrm{ppX}$. For this, events with exactly two tracks registered in the drift chambers D1, D2 and the scintillation hodoscopes S1, S3 were selected (see Fig. 5.1). The proton identification technique was the same as in the analysis of the kaons production and was based on the ToF measurement for particles registered in the S1 and S3. Figure 5.2 presents invariant mass squared of particles registered in the S1 and S3 hodoscopes for the simulations and for the experimental data, together with the range chosen for identification of protons. The π^+ peak in the spectrum from the simulations comes only from the ω decay, but the one in the experimental spectrum can also be manifestation of other (background) reactions.

After selection of events with two identified protons, the missing mass of the two-proton system was calculated as follows:

$$m_{\mathrm{miss}} = \sqrt{(E - \sum_{i=1}^{2} E_i)^2 - (\sum_{i=1}^{2} p_{x_i})^2 - (\sum_{i=1}^{2} p_{y_i})^2 - (p_{\mathrm{beam}} - \sum_{i=1}^{2} p_{z_i})^2}. \qquad (5.1)$$

The resulting missing-mass distribution is presented in Fig. 5.3. In the distribution, clear signals coming from the production of ω(782) and η'(958) mesons lying on top of multi-pion background are visible.

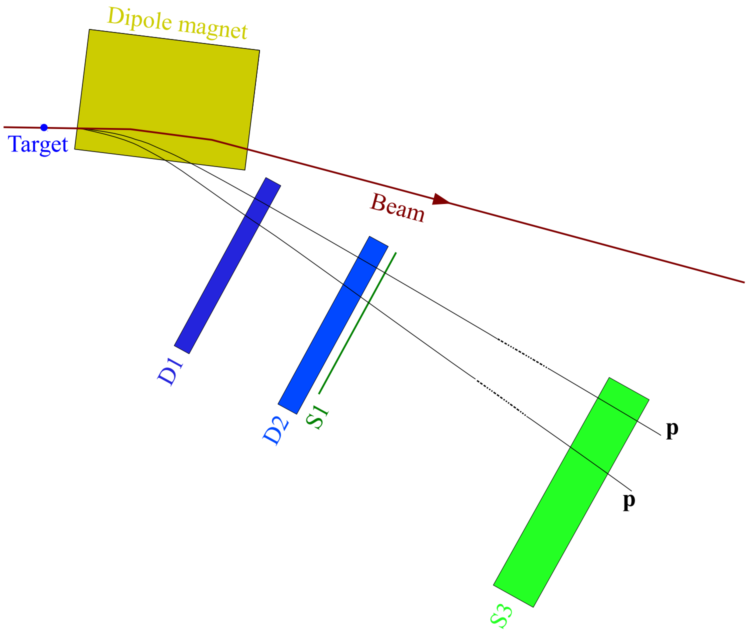

Figure 5.1: Principle of the pp → ppX measurement with the COSY-11 detection system.

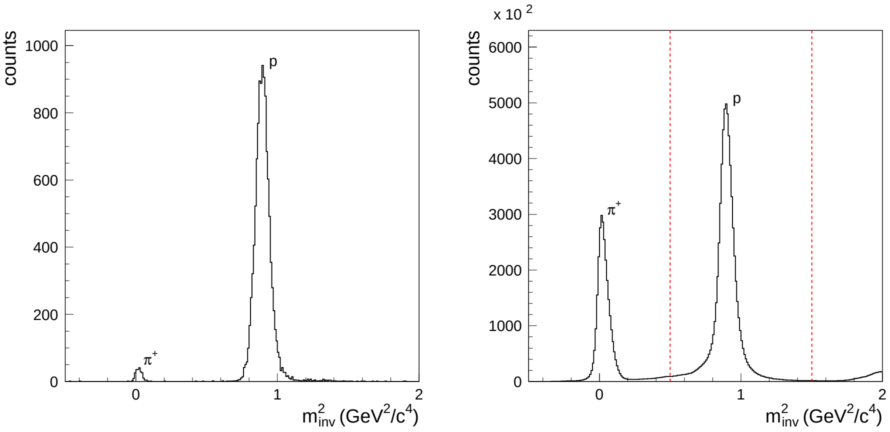

Figure 5.2: Invariant mass squared of particles registered in the S1 and S3 hodoscopes for simulations of the pp → ppω reaction (left) and for the measured data (right). Red lines present a range selected for the protons identification.

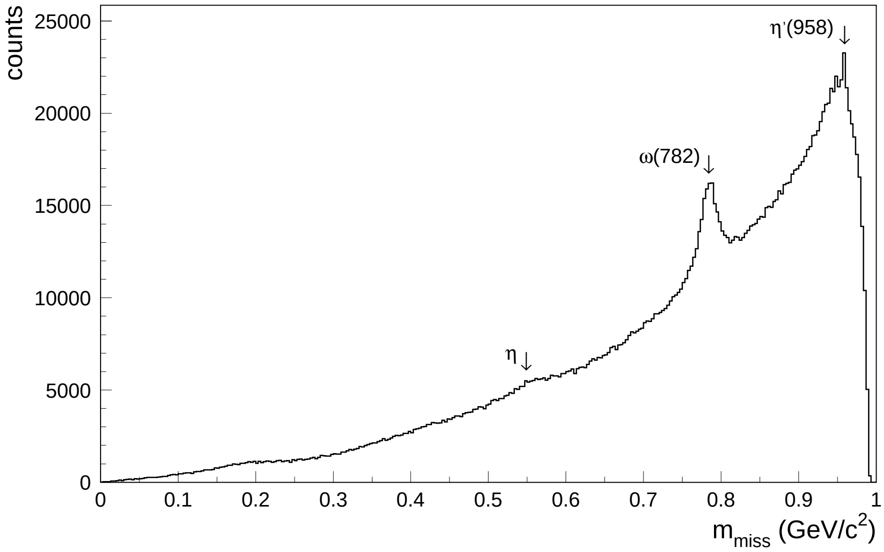

Figure 5.3: Missing-mass spectrum of the two-proton system with visible signals at masses of the ω(782) and η'(958) mesons.

5.2 Total cross section for the ω meson production

For subtraction of the background under the ω meson peak in the missing-mass spectra, a fit of 2^{nd} order polynomial to the background was used (see Fig. 5.4). Obtained in this way number of events in the ω meson peak was 37807.

The acceptance of the detection system for the $pp \to pp\omega$ reaction, calculated using the Monte Carlo simulation, is 0.061%. The resulting total cross section for the ω production at the excess energy Q = 210 MeV equals 41.6 ± 8.3 μb. The uncertainty of the cross section includes the uncertainty of the integrated luminosity and the uncertainty of the background subtraction which was estimated by fitting polynomials of various orders to the background. The present data point is in a good agreement with results of previous experiments and the theoretical prediction within the one-pion exchange model of Ref. [50], as shown in Fig. 5.5. However, it is not in an agreement with (unpublished) results obtained during one of the previous COSY-11 experiments [51].

5.3 Total cross section for the η' meson production

The η' peak in the proton-proton missing-mass spectrum lies on a high background corresponding to the multi-pion production, which is presented on the left-hand side of Fig. 5.6. The number of counts in the peak, obtained after subtraction of the background fitted with

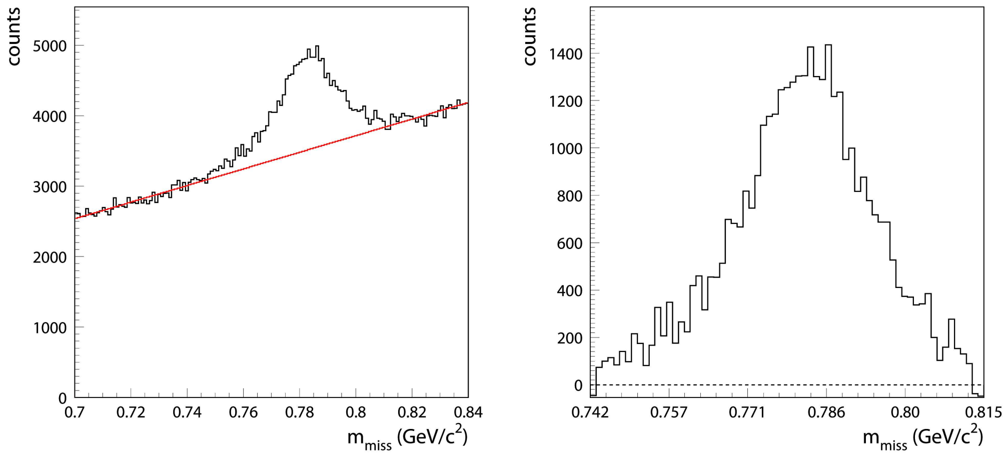

Figure 5.4: Two-proton missing-mass distribution in ω region (left). Red line presents the 2nd order polynomial fit used for the background subtraction. Peak corresponding to the ω production after the background subtraction (right).

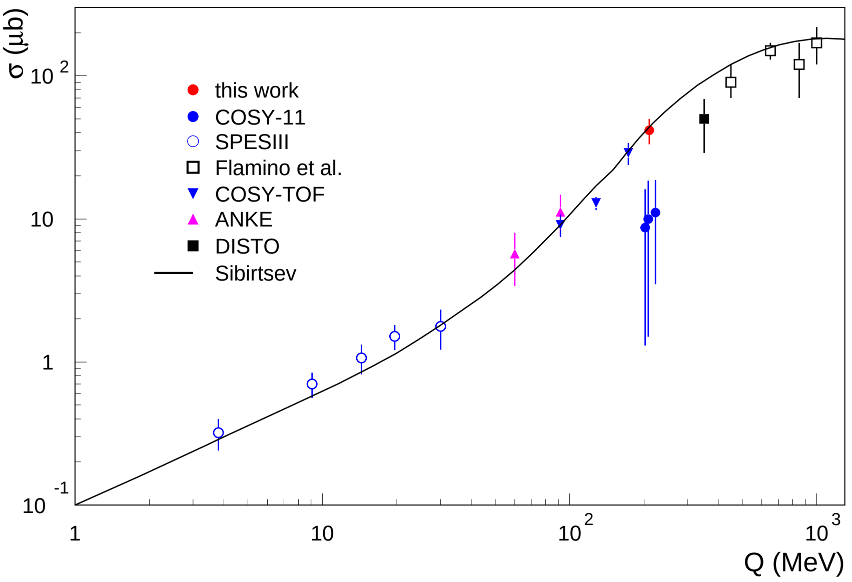

Figure 5.5: Total cross section for the pp → ppω reaction obtained in the present measurement together with results from other measurements [43, 51–55]. Solid line presents theoretical prediction for the ω production cross section from Ref. [50].

2^{nd} order polynomial (see right-hand side of Fig. 5.6), is equal to 3199.

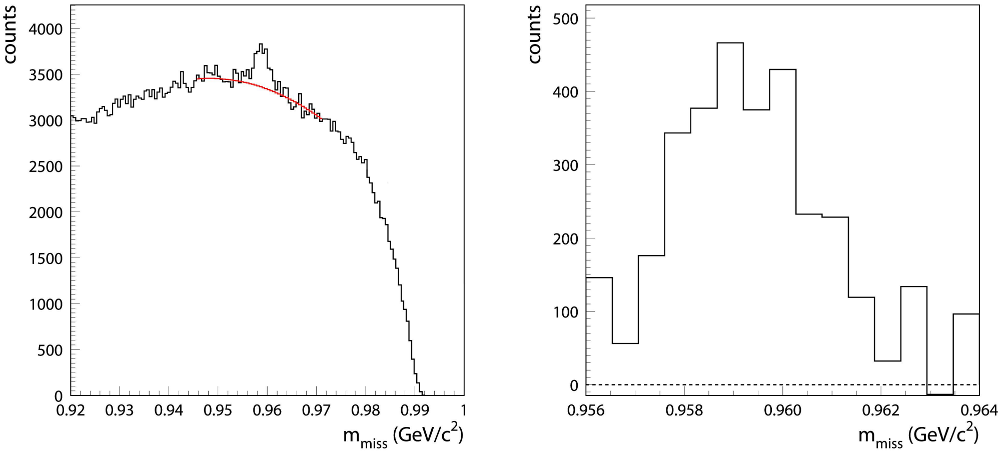

Figure 5.6: Two-proton missing-mass distribution in the η' region (left). Red line presents the 2^{nd} order polynomial fit used for the background subtraction. The η' peak after the background subtraction (right).

The COSY-11 acceptance for the pp → ppη' reaction at the excess energy Q = 34 MeV, corresponding to the beam momentum of the present measurement (3.316 GeV/c), is equal to 0.67%. The acceptance was determined using the simulations of the pp → ppη' reaction with the FSI in the proton-proton system included.

The resulting total cross section for the pp → ppη' reaction is equal to 335 ± 61 nb. The uncertainty of the cross section includes the uncertainty of the integrated luminosity and the uncertainty of the background subtraction which was estimated by fitting polynomials of various orders to the background.

The obtained value is in a good agreement with results of previous experiments and with the theoretical model of the final-state interaction of Ref. [3], as shown in Fig. 5.7.

The agreement of the present cross sections for the ω and η' meson production with results of other measurements confirms the correctness of the determination of luminosity.

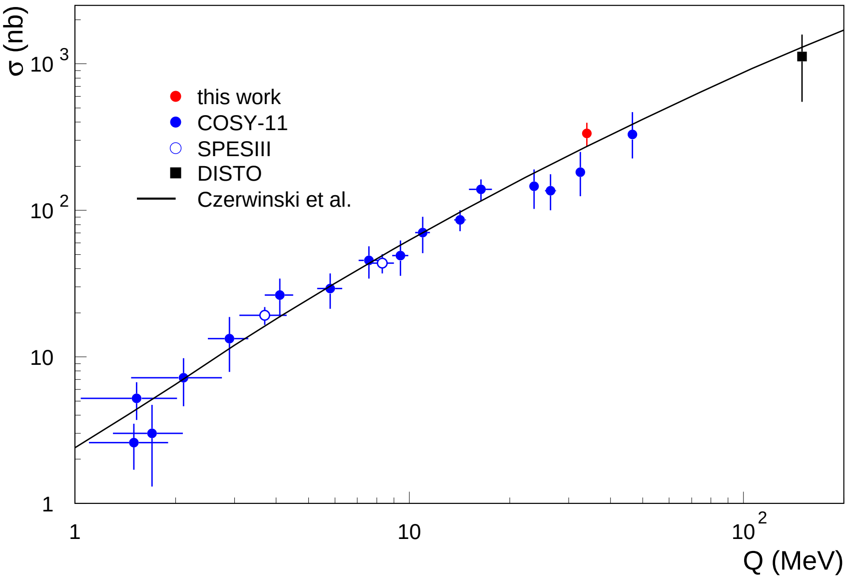

Figure 5.7: Total cross section for the pp → ppη' reaction obtained in the present experiment together with results from other measurements [9, 56–61]. Solid line presents theoretical prediction for the η' production cross section from Ref. [3].

Chapter 6

Summary

The aim of this work was to measure the total cross section for the $pp \rightarrow ppK^+K^-$ reaction very close to threshold, at an excess energy of only 4.5 MeV. The expectation was that this data point, together with experimental data available at higher energies above the threshold, should allow more precise determination of the pK^- and K^+K^- interactions in the final state. Knowledge of this interaction is important for understanding the structure of the $\Lambda(1405)$ hyperon which is considered as pK^- bound state, and of the $f_0(980)$ and $a_0(980)$ mesons - possible kaonic molecules.

The measurement was performed at the COSY accelerator using the COSY-11 detection system. The COSY proton beam with momentum of 3.316 GeV/*c*, was scattered on an internal H_2 cluster target. The positively charged products of the $pp \rightarrow ppK^+K^-$ reaction (two protons and K^+) were registered in a set of drift chambers and scintillation hodoscopes. Their momenta were determined based on deflection of their trajectories in the magnetic field of the COSY-11 dipole magnet and their identification was based on the time of flight measured with the scintillation hodoscopes. For identification of the negatively charged kaons, the missing-mass method was used.

In the experiment, the luminosity was monitored by a coincident measurement of the elastically scattered protons. The integrated luminosity, determined by comparison of the registered counts, corrected for the detector acceptance, with the high precision proton-proton elastic cross sections measured by the EDDA collaboration, was 1.52 pb^{-1}.

The trigger applied in the experiment allowed the registration of reactions of the type $pp \rightarrow ppX$ where X is one or more mesons. In the missing-mass spectrum of the two outgoing protons, clear peaks from the ω and η' meson production are visible. This allowed the determination of the total cross section for the production of the ω meson to be equal to 41.6 ± 8.3 μb at the excess energy Q = 210 MeV, and of the η' to be equal to 335 ± 61 nb at Q = 34 MeV. The total cross section for the ω meson production is in a good agreement with theoretical predictions based on the one-pion exchange model of Ref. [50]. Also the total cross section for the η' production agrees with data points from other experiments and with the theoretical model of the final-state interaction of Ref. [3].

In the collected data, no ppK^+K^- events were found, and therefore only an upper limit for the $pp \to ppK^+K^-$ total cross section at the excess energy of 4.5 MeV was determined. It equals 0.070 nb at 95% level of confidence. This upper limit lies below the theoretical prediction of Ref. [28] which takes into account the pp, pK^- and K^+K^- FSI and well describes the experimental data at higher energies. The observed deviation can result from the Coulomb interaction between the final-state particles, which was not fully included in the theoretical calculations, or can be caused by the strong absorption of the K^+K^- pairs due to formation of the hypothetical $K\bar{K}$ molecule [4].

References

[1] S. Brauksiepe *et al.*, Nucl. Instr. and Meth. A **376**, 397 (1996)
[2] D. Schröer *et al.*, EPJ Web of Conferences **130**, 03008 (2016)
[3] E. Czerwiński *et al.*, Phys. Rev. Lett. **113**, 062004 (2014)
[4] C. Wilkin, Eur. Phys. J. A **53**, 114 (2017)
[5] J.D. Weinstein and N. Isgur, Phys. Rev. D **41**, 2236 (1990)
[6] R. Dalitz *et al.*, Phys. Rev. **153**, 1617 (1967)
[7] M. Wolke, Ph.D. thesis, Rheinische Friedrich-Wilhelms-Universität, Bonn (1997)
[8] F. Balestra *et al.*, Phys. Lett. B **468**, 7 (1999)
[9] C. Quentmeier *et al.*, Phys. Lett. B **515**, 276 (2001)
[10] P. Winter *et al.*, Phys. Lett. B **635**, 23 (2006)
[11] Q.J. Ye *et al.*, Phys. Rev. C **87**, 065203 (2013)
[12] C. Patrignani *et al.* (Particle Data Group), Chin. Phys. C **40**, 100001 (2016)
[13] R.L. Jaffe, Phys. Rev. D **15**, 267 (1977)
[14] A. Deandrea *et al.*, Phys. Lett. B **502**, 79 (2001)
[15] T. Hyodo and D. Jido, Prog. Part. Nucl. Phys. **67**, 55 (2012)
[16] J.M.M. Hall *et al.*, Phys. Rev. Lett. **114**, 132002 (2015)
[17] B. Borasoy *et al.*, Eur. Phys. J. A **25**, 79 (2005)
[18] M. Bazzi *et al.*, Nucl. Phys. A **881**, 88 (2012)
[19] A.D. Lahiff, PiN Newslett. **16**, 385 (2002)
[20] J. Zmeskal, Progress in Part. and Nucl. Phys. **61**, 512 (2008)
[21] O.V. Doce *et al.*, Phys. Lett. B **758**, 134 (2016)
[22] P. Senger *et al.*, Prog. Part. Nucl. Phys. **42** 209 (1999)
[23] P. Moskal *et al.*, J. Phys. G **28**, 1777 (2002)
[24] Y. Maeda *et al.*, Phys. Rev. C **77**, 01524 (2008)
[25] K.M. Watson, Phys. Rev. **88**, 1163 (1952)
[26] M. Goldberger and K.M. Watson, Collision Theory, Wiley, New York (1964)
[27] L. Schiff, Quantum Mechanics, McGraw-Hill, New York (1968)
[28] M. Silarski and P. Moskal, Phys. Rev. C **88**, 025205 (2013)
[29] Y. Yan, arXiv:0905.4818
[30] R. Maier, Nucl. Instr. and Meth. A **390**, 1 (1997)
[31] J. Dietrich *et al.*, Instrum. Exp. Tech. **46**, 581 (2003)
[32] D. Prasuhn *et al.*, Nucl. Instr. and Meth. A **441**, 167 (2000)
[33] H. Dombrowski *et al.*, Nucl. Instr. and Meth. A **386**, 228 (1997)

[34] A. Khoukaz *et al.*, Eur. Phys. J. D **5**, 275 (1999)
[35] T. Rożek, Ph.D. thesis, Uniwersytet Śląski, Katowice (2005)
[36] M. Sokołowski *et al.*, Annual Report IKP-KFA 1990, 219 (1991)
[37] G. Anton *et al.*, Nucl. Instr. and Meth. A **310**, 631 (1991)
[38] P. Moskal, Ph.D. thesis, Uniwersytet Jagielloński, Kraków (1998)
[39] M. Köhler *et al.*, Tech. Rep., Jül-3071 (1995)
[40] K. Zwoll *et al.*, IEEE Trans. Nucl. Sci. **41**, 37 (1994)
[41] A. Breskin *et al.*, Nucl. Instr. and Meth. **119**, 9 (1974)
[42] J.S. Siebenson Ph.D. thesis, Technische Universität München (2013)
[43] V. Flaminio *et al.*, Compilation of Cross-Sections, CERN-HERA, 84 (1984)
[44] M. Abdel-Bary *et al.*, Eur. Phys. J. A **46**, 27 (2010)
[45] D. Albers *et al.*, Eur. Phys. J. A **22**, 125 (2004)
[46] R.L. Workman *et al.*, http://gwdac.phys.gwu.edu, Phys. Rev. C **94**, 065203 (2016)
[47] J.P. Naisse *et al.*, Nucl. Phys. A **278**, 506 (1977)
[48] Q-F. Lü *et al.*, Phys. Rev. C **90**, 034002 (2014)
[49] J.A. Oller and E. Oset, Nucl. Phys. A **620**, 438 (1997)
[50] A.A. Sibirtsev *et al.*, Phys. Rev. Lett. **80**, 3202 (1998)
[51] C. Quentmeier, Ph.D. thesis, Westfälische Wilhelms-Universität, Münster (2001)
[52] F. Hibou *et al.*, Phys. Rev. Lett. **83**, 492 (1999)
[53] F. Balestra *et al.*, Phys. Rev. C **63**, 024004 (2001)
[54] S. Abd El-Samad *et al.*, Phys. Lett. B **522**, 16 (2001)
[55] M. Abdel-Bary *et al.*, Phys. Lett. B **647**, 351 (2007)
[56] P. Moskal *et al.*, Phys. Rev. Lett. **80**, 3202 (1998)
[57] F. Hibou *et al.*, Phys. Lett. B **438**, 41 (1998)
[58] P. Moskal *et al.*, Phys. Lett. B **474**, 416 (2000)
[59] F. Balestra *et al.*, Phys. Lett. B **491**, 29 (2000)
[60] A. Khoukaz *et al.*, Eur. Phys. J. A **20**, 345 (2004)
[61] P. Klaja *et al.*, Phys. Lett. B **684**, 11 (2010)

Acknowledgements

I would like to thank many people I had a great pleasure to work with or to meet during the preparation of this thesis.

First of all I would like to express my gratitude to Prof. Walter Oelert and Prof. Paweł Moskal for giving me an opportunity to work in the COSY-11 collaboration at the Jülich Research Centre.

I wish to thank all the other members of the collaboration, especially those whose work during the data taking in October 2005 was essential to obtain the data which were the basis of this thesis: Joanna Przerwa, Paweł Klaja, Dieter Grzonka, Rafał Czyżykiewicz, Tomek Rożek, Thomas Sefzick, Alexander Täschner, Heinz-Hermann Adam, Zhangdong Zhang, Michał Janusz, Peter Winter, Eryk Czerwiński and Marek Siemaszko. And others whose work during all the years before my joining the collaboration has enabled me to investigate kaons production at the COSY-11 detection system.

I am indebted to the Director of IKP-1 Prof. James Ritman for his hospitality and the whole COSY team for providing a good quality beam during the experiment.

For the time spent on careful reading of this dissertation my gratitude is due to Prof. Colin Wilkin. His suggestions and corrections were always very essential and to-the-point. He deserves my thanks also for his patience in answering all of my questions.

This Ph.D. was supported in part from funds of the Polish National Science Centre within the project UMO-2014/15/B/ST2/00049.

Podziękowania

Za gościnność, okazaną mi podczas pracy nad niniejszą rozprawą przez Zakład Fizyki Jądrowej, dziękuję wszystkim jego kierownikom, którzy mi jej udzielili: prof. dr. hab. Reinhardowi Kulessie, prof. dr. hab. Bogusławowi Kamysowi oraz prof. dr. hab. Pawłowi Moskalowi.

Profesorowi dr. hab. Lucjanowi Jarczykowi jestem wdzięczny za wszystkie rady, komentarze, pytania oraz dyskusje podczas seminariów i przy innych okazjach, zmuszające do wysiłku intelektualnego i pełniejszego zrozumienia zarówno zagadnień fizycznych, jak i tych związanych z analizą danych.

Wszystkim pozostałym pracownikom naukowym zakładu, dziękuję za ciągłą gotowość do okazania wszelkiej potrzebnej mi pomocy.

Za udzielone wsparcie i szczególną wyrozumiałość podczas ostatniego etapu przygotowywania pracy dziękuję prof. dr. hab. Elżbiecie Richter-Wąs.

Nie jestem w stanie wymienić wszystkich pracowników technicznych i administracyjnych pracujących na Wydziale Fizyki, Astronomii oraz Informatyki Stosowanej, których codzienna praca była niezbędna abym mógł napisać niniejszą pracę, dlatego podziękowania dla nich wszystkich kieruję na ręcę kilku osób, z którymi miałem najczęstszy kontakt: Krystyny Szałkowskiej, Alicji Mysłek, Barbary Kozak, Agnieszki Wach oraz Wojtka Migdała.

Za wspólnie spędzony czas dziękuję osobom, z którymi na przestrzeni kilku lat dzieliłem pokój w instytucie: Piotrkowi, Adrianowi, Wojtkowi, Michałowi i Bartkowi.

Miałem wyjątkowe szczęście spotkać w Instytucie Fizyki wiele niezwykłych koleżanek i kolegów, spośród których szczególnie ciepło wspominam Magdę, Anię, Witka, Jacka, Tomka, Marcina, Sławka, Roberta, Andrzeja i Mariusza.

Niektóre z poznanych w trakcie studiów doktoranckich osób towarzyszą mi także w życiu poza uczelnią jako moi przyjaciele. Agato, Beato, Dagmaro, Gosiu, Marto, Olu, Radku, Łukaszu, Nikodemie, Marku, Mariuszu, Piotrze i Lechu, nawet gdybym nigdy nie ukończył tej pracy, fakt że dzięki niej Was poznałem powoduje, że nie żałowałbym jej podjęcia.

Na końcu pragnę wyrazić głęboką wdzięczność najważniejszej osobie, bez której niniejsza rozprawa by nie powstała, mojemu promotorowi prof. dr. hab. Jerzemu Smyrskiemu. Dziękuję za podarowaną szansę prowadzenia badań pod Pana kierunkiem, a w szczególności za okazaną cierpliwość. Bez Pana wysiłku, popartego ogromnym doświadczeniem oraz wiedzą, nigdy nie uzyskałbym żadnych wyników. Dziękuję również za ogromną ilość czasu poświęconą na dopracowanie tekstu niniejszej rozprawy do formy, która pozwala na jej opublikowanie.

Największe podziękowania należą się jednak osobom, bez których nigdy niczego bym nie osiagnął. To oni wpoili we mnie ciekawość świata oraz jako pierwsi cierpliwie odpowiadali na każde moje pytanie na jego temat. Mamo, Tato nie wyobrażam sobie lepszych rodziców, dziękuję za wszystko. Kocham Was.